

# UC San Diego

## UC San Diego Previously Published Works

### Title

Decadal-scale variations in geomagnetic field intensity from ancient Cypriot slag mounds

### Permalink

<https://escholarship.org/uc/item/6j97s4mq>

### Journal

Geochemistry, Geophysics, Geosystems, 16(1)

### ISSN

15252027

### Authors

Shaar, Ron  
Tauxe, Lisa  
Ben-Yosef, Erez  
[et al.](#)

### Publication Date

2015

### DOI

10.1002/2014GC005455

Peer reviewed

1 **Decadal-scale variations in geomagnetic field intensity from ancient Cypriot slag**  
2 **mounds**

3

4 Ron Shaar<sup>1\*</sup>, Lisa Tauxe<sup>1</sup>, Erez Ben-Yosef<sup>1,2</sup>, Vasiliki Kassianidou<sup>3</sup>, Brita Lorentzen<sup>4</sup>,  
5 Joshua M. Feinberg<sup>5,6</sup>, Thomas E. Levy<sup>7</sup>

6 <sup>1</sup> Scripps Institution of Oceanography, University of California, San Diego, La Jolla,  
7 California, 92093-0220, USA.

8 <sup>2</sup> Department of Archaeology and Ancient Near Eastern Cultures, Tel Aviv University,  
9 Tel Aviv, Israel.

10 <sup>3</sup> Department of History and Archaeology, University of Cyprus, Nicosia, Cyprus.

11 <sup>4</sup> Cornell Tree-Ring Laboratory, Cornell University, Ithaca, NY 14853, USA.

12 <sup>5</sup> Institute for Rock Magnetism, Department of Earth Sciences, University of Minnesota,  
13 Minneapolis, MN 55455, USA.

14 <sup>6</sup> Department of Anthropology, University of Minnesota, Minneapolis, MN 55455, USA.

15 <sup>7</sup> Department of Anthropology, University of California San Diego, La Jolla, CA, USA.

16

17 \* Corresponding author. E-mail: [rshaar@ucsd.edu](mailto:rshaar@ucsd.edu)

18

19 **Key Points**

- 20 • Decadal scale paleointensity data from ancient slag mounds in Cyprus.  
21 • High paleointensity rate of change during the 5<sup>th</sup> century CE.  
22 • Levant and south Africa may be longitudinally-paired active areas

23

24 **Abstract**

25 Geomagnetic models based on direct observations since the 1830s show that the relative  
26 decadal rate of change in field intensity on Earth's surface over the past 170 years is less  
27 than 4.8% per decade. It is unknown if these rates represent the typical behavior of  
28 secular variations due to insufficient temporal resolution of archaeomagnetic records  
29 from earlier periods. To address this question we investigate two ancient slag mounds in  
30 Cyprus - Skouriotissa Vouppes (SU1, 4<sup>th</sup> to 5<sup>th</sup> centuries CE, 21 meter in height), and  
31 Mitsero Kokkinoyia (MK1, 7<sup>th</sup> to 5<sup>th</sup> BCE, 8 meter in height). The mounds are multi-

32 layered sequences of industrial slag and charcoals that accumulated near ancient copper  
33 production sites. We collected geo-referenced slag and charcoals from vertical sections  
34 excavated from the mounds, and generated two independent sub-century scale  
35 paleointensity time series. We modeled the age-height relation using radiocarbon dates,  
36 and estimated paleointensities using Thellier-type IZZI experiments with additional  
37 anisotropy, cooling rate, and non-linear TRM assessments. To screen out non single-  
38 domain data with ambiguous interpretations we applied strict selection criteria at the  
39 specimen/sample levels. To ensure objectivity, consistency, and robust error estimation  
40 we employed an automatic interpretation technique and put all the data available in the  
41 MagIC database. Only a small percentage of the samples yielded satisfying behavior but  
42 they provide highly reliable paleointensity estimates. Eleven indistinguishable estimates  
43 from MK1 indicate relatively stable field at the time the mound accumulated. However,  
44 ten paleointensity estimates from SU1 demonstrate a rate of change comparable to the  
45 highest rate in the historical field anywhere on Earth. We suggest that high secular  
46 variations rates observed in the ancient Levant are not coincidental. Geomagnetic models  
47 from the past 170 years show two longitudinally-paired geomagnetically active regions:  
48 the Middle East and South Africa. This analysis implies a link to persistently active  
49 quasi-stationary columnar convection cells.

50

51

## 52 **Index Terms**

53 1503 Archeomagnetism

54 1521 Paleointensity

55 1522 Paleomagnetic secular variation

56 1530 Rapid time variations

57

## 58 **Keywords**

59 paleointensity, archaeointensity, archaeomagnetism, geomagnetic secular variations, slag

60

## 61 **1 Introduction**

62 Changes in the geomagnetic field that occur over short time scales are referred to as  
63 geomagnetic secular variation (SV). One fundamental characteristic of SV, still not fully  
64 understood, concerns the shortest time scale for significant changes in field intensity.  
65 Direct measurements of field intensity that go back to 1832 (Malin and Barraclough,  
66 1982) show relatively small changes with rather smooth behavior over decadal timescales  
67 (e.g. Cafarella et al., 1992; Barraclough et al., 2000). In contrast, recent archaeomagnetic  
68 studies have revealed periods with significant intensity variations over decadal to  
69 centennial time scales (Gallet et al., 2003, Ben-Yosef et al., 2009; Genevey et al., 2009;  
70 Shaar et al., 2011, Gómez-Paccard et al., 2012). This apparent inconsistency suggests that  
71 temporal variations in the geomagnetic field intensity over the past two centuries have  
72 been relatively small compared to earlier periods. To investigate this question, high-  
73 resolution paleointensity records from periods preceding those covered by direct  
74 geomagnetic observations are required.

75 Obtaining sub-century scale paleointensity records is a difficult task. First, the studied  
76 material needs to fulfill a strict list of requirements (e.g., Dunlop and Özdemir, 2001;  
77 Valet, 2003; Tauxe and Yamazaki, 2007), such as having a pure thermoremanent  
78 magnetization (TRM) carried exclusively by single-domain (SD) like particles. In  
79 addition, paleointensity experiments should be carefully designed using sufficient number  
80 of specimens (Paterson et al., 2010), and with accurate corrections for remanence  
81 anisotropy (Rogers et al., 1979; Selkin et al., 2000; Kovacheva et al., 2009), cooling rate  
82 effects (e.g. Genevey and Gallet, 2002; Ferk et al., 2014), and non-linear TRM (Selkin et  
83 al., 2007; Shaar et al., 2010). Furthermore, as the interpretations of the paleointensity  
84 experimental data can be non-unique a robust data analysis methodology is required to  
85 ensure comparability, objectivity, and robust assessment of error estimation (Shaar and  
86 Tauxe, 2013). Finally, above all, achieving the desired resolution in age is difficult and  
87 often impossible.

88 This study pursues the challenge of obtaining sub century scale paleointensity records  
89 using ancient copper slag mounds (e.g. Kassianidou, 2004, Levy et al., 2008; Ben-Yosef  
90 et al., 2009; Shaar et al., 2011). Copper slag mounds are industrial waste mounds  
91 consisting of slag and charcoals (the main side product of copper smelting procedure)



92 that accumulated as long as copper was produced in nearby smelting sites. Copper slag  
93 mounds afford a unique opportunity for obtaining virtually continuous high resolution  
94 paleointensity time series.

95 The first paleointensity investigation of Levantine copper slag material was conducted by  
96 Ben-Yosef et al. (2008a,b) who recognized the diversity of slag types, and demonstrated  
97 that some types of slag are suitable paleointensity source material. Based on this research  
98 Shaar et al. (2010) examined the rock magnetic properties of selected slag material from  
99 Timna valley, Israel, and concluded that Timna's glassy slag contain populations of  
100 single domain (SD) like grains ideal for paleointensity studies. Using synthetic re-melted  
101 Fe-rich slag Shaar et al. (2010) estimated the **accuracy** of the paleointensity procedure on  
102 SD-like samples to be better than 6%. Later, Shaar and Feinberg (2013) demonstrated  
103 that the SD-like properties are due to sub-micrometer scale dendritic structures in the  
104 ferromagnetic minerals. Based on these findings Ben-Yosef et al. (2009) and Shaar et al.  
105 (2011) investigated contemporaneous slag mounds in Timna valley, Israel and in Khirbat  
106 En Nahas, Jordan, and constructed a decadal scale paleointensity time series for the Iron  
107 Age.

108 In this study we follow the approach presented in our previous studies, and investigate  
109 two slag mounds in Cyprus from the Late Iron Age / Classical period (ca. 7<sup>th</sup> – 5<sup>th</sup>  
110 centuries BCE) and the Late Roman / Byzantine Period (ca. 4<sup>th</sup> – 5<sup>th</sup> centuries CE). The  
111 aim of this study is to obtain new decadal scale paleointensity time series of the periods  
112 represented by the Cypriot slag mounds.

113

## 114 **2 Methods**

### 115 **2.1 Archaeomagnetic sampling**

#### 116 Skouriotissa Vouppes (SU1) slag mound

117 The Skouriotissa copper mine is located near one of the major copper ore deposits in  
118 Cyprus and is the largest and longest-lived active copper mine on the island. Copper ores  
119 were extensively mined in this area through the Roman Era, leaving behind enormous  
120 slag mounds in the surrounding hills. The SU1 slag mound (35.093018°N, 32.885336°E,  
121 Figs. 1,2) is one of the largest Late Roman / Byzantine Era slag mounds. It is located at

122 the southern flank of the modern open pit mine and was partially exposed by road  
123 construction. The slag at SU1 is characterized by large slag pieces up to a few tens of  
124 centimeters across and up to ten centimeters in thickness (Fig. S1, Supplementary  
125 Material). The top part of the slag pieces is frequently glassy and exhibits vesicles and  
126 flow textures. Many of these large chunks were crushed to smaller pieces before they  
127 were dumped in the mound. Charcoal fragments ranging in size from a few mm to a few  
128 centimeters are abundant throughout the entire section (Fig. S1, Supplementary Material).

129 Figure 2 shows a cross-section of SU1. Our excavations followed an existing exposed  
130 outcrop near the road cut, here marked as 'step 6'. The part below step 6 was excavated  
131 to a section of laminated clay sediments that defines the base of the mound (step 7). The  
132 part above step 6 was divided to five steps ~2 m in height (step 1-5). All steps were  
133 vertically leveled, cleaned, and divided into loci (archaeological layers) by visible  
134 horizons (dashed lines in Fig. 2). We collected more than 400 pieces of slag, over 300  
135 charcoal fragments, and 21 baked clay objects from the cleaned outcrops. The samples  
136 were collected from 118 different locations in 36 different loci as shown in Figure 2. The  
137 3D coordinates of each sampling location and loci boundaries were measured and  
138 recorded using a Total Station, allowing documentation with a spatial resolution of better  
139 than 5 cm. The total height of the studied section, as measured by the Total Station, is  
140 21.1m.

#### 141 Mitsero Kokkinoyia (MK1)

142 Mound MK1 (35.042130°N, 33.106650°E, Figs 1,3) is located near the copper mines in  
143 the Mitsero Kokkinoyia area. Previous studies dated the activity here to the 7<sup>th</sup> to 3<sup>rd</sup>  
144 centuries BCE, i.e., the Late Iron Age in Cyprus (Kassianidou, 2004). The section is 8  
145 meters in height and contains a complicated sequence of slag layers separated by soil  
146 layers. Several unconformities near Loci 15, 25, 27, and 32 (Fig. 3) suggest a complex  
147 history of accumulation. More than 200 pieces of slag and over 60 charcoal fragments  
148 were collected from 101 sampling locations. Nine soil layers were sampled for charcoal  
149 flotation analysis (Loci 5, 8, 12, 14, 15, 21, 23, 27, 32). Sampling locations and loci  
150 boundaries were recorded using a Total Station.

151 **2.2 Wood identification and radiocarbon dating**

152 Wood identification of the charcoal was done at the Cornell Tree-Ring Laboratory at  
153 Cornell University. Each charcoal section was fractured with a razor blade to create fresh  
154 transverse, radial, and tangential planes (following Cartwright and Parkington, 1997).  
155 The samples were examined under an Olympus Bx41 binocular microscope and Motic K-  
156 400P stereo microscope at magnifications up to x500. The characteristic features of the  
157 wood were documented, photographed, and then compared with archaeological and  
158 modern wood reference collections, standard reference texts (Fahn et al., 1986;  
159 Schweingruber, 1990; Akkemik and Yaman, 2012), and the InsideWood anatomical  
160 database (<http://insidewood.lib.ncsu.edu/>). In some cases, it was possible to identify  
161 samples only to the family or genus level, because of either physical changes to the  
162 cellular morphology from the charring process or indistinguishable anatomical features  
163 among species in the same genus or subgenus.

164 Nineteen charcoal samples - eleven from SU1 and eight from MK1 - were selected for  
165 radiocarbon dating. Seventeen of these samples are pine (*Pinus* sp.) and are most likely  
166 *Pinus brutia* Ten. One of the samples is an evergreen oak (*Quercus section Ilex*). Since  
167 the mounds did not contain clearly short-lived material (like seeds), the outer rings of  
168 branch and twig samples with bark were extracted when possible for the radiocarbon  
169 analysis to minimize old wood bias. AMS radiocarbon measurements were done at the  
170 NSF Arizona AMS laboratory, University of Arizona. Dates were calibrated and modeled  
171 using OxCal v.4.2.3 (Ramsey, 2009) and compared against the IntCal13 calibration curve  
172 (Reimer et al., 2013).

173 **2.3 Paleointensity experiments**

174 Paleointensity experiments were carried out at the paleomagnetic laboratory of Scripps  
175 Institution of Oceanography (SIO), University of California San Diego. Samples were  
176 prepared by cutting chips of 1-5 mm in size from the glassy part of the slag. The chips  
177 were wrapped in glass filter paper and glued inside 12 mm diameter glass vials using  
178 potassium-silicate glue (KASIL). The experimental procedure followed the IZZI protocol  
179 of Tauxe and Staudigel (2004) with routine pTRM checks (Coe et al., 1978) at every

180 second temperature step. The oven field was set to 40 or 60  $\mu\text{T}$ . In total, 673 specimens  
181 from 153 samples were analyzed.

182 Remanence anisotropy tensors were calculated using thermoremanent magnetizations or  
183 anhysteretic remanent magnetizations (ATRM and AARM, respectively). The ATRM  
184 procedure included 8 heating steps carried out at the highest temperature that the  
185 specimens reached during the Thellier experiment: a baseline step in a zero field  
186 (subtracted from the subsequent infield measurements), six infield steps in 60  $\mu\text{T}$  at  
187 orthogonal directions (+x, +y, +z, -x, -y, -z), and an additional infield alteration check at  
188 the end of the experiment. AARM was done in 9 positions following the scheme of  
189 Jelinek (1978, see also Tauxe, 2010) using 180 mT AC field and 100  $\mu\text{T}$  DC field. Before  
190 each ARM step, the specimen was AF demagnetized at 180 mT and this baseline  
191 magnetization was measured and subtracted from the subsequent infield ARM  
192 measurement. Anisotropy tensors were calculated using the method of Hext (1963, see  
193 also Tauxe, 2010) via PmagPy software (Tauxe, 2010).

194 Non-linear TRM (NLT, Selkin et al., 2007) was checked on 167 specimens using 4-5  
195 infield steps carried out at the highest temperature of the Thellier experiment in oven  
196 fields ranging from 20 to 80  $\mu\text{T}$ . The results demonstrated that the NLT effect is  
197 insignificant (see Section 3.2), and therefore, the rest of the specimens were not subjected  
198 to the NLT procedure.

199 Cooling rate effect was tested on four specimens from the only baked clay sample in this  
200 study (su102501a). The cooling rate experiment included four steps in 590°C: zero-field  
201 step (for baseline measurement), infield step at 60 $\mu\text{T}$  in regular (fast) cooling rate (Figure  
202 S2, Supplementary Material), infield step at 60 $\mu\text{T}$  in a slow cooling rate (Figure S2,  
203 Supplementary Material), and infield step at regular cooling rate (alteration check).  
204 Cooling rare correction (Figures S3,S4, Supplementary Material) was calculated  
205 assuming the relation between TRM and cooling rate given in Halgedahl et al. (1980),  
206 assuming an averaged ancient cooling rate of 6 hours from 500°C to 200°C.

## 207 **2.4 Paleointensity data analyses and interpretation procedures**

208 The conventional technique for interpreting paleointensity data is to manually pick  
209 temperature bounds for each specimen separately. The selected temperature bound is

210 somewhat arbitrary and reflects some subjective consideration for what is assumed to be  
211 the most appropriate temperature interval. The quality of the interpretation is commonly  
212 quantified by paleointensity statistics (e.g. Paterson et al., 2014) that assess different  
213 aspects of the experimental behavior. Paleointensity statistics are often used as selection  
214 criteria by assigning threshold values to each statistic. As specimen interpretations alone  
215 are insufficient to account for all sources of uncertainty the final paleointensity estimate  
216 is usually calculated as a sample (cooling unit) mean or as a site (collection of samples of  
217 the same age) mean. The standard deviation of the mean is usually reported as the error  
218 bounds of the paleointensity estimate.

219 Despite the known benefits of the conventional approach for paleointensity interpretation,  
220 it has some important drawbacks. One root problem is that there is no consensus on  
221 which selection criteria and which threshold values should be used in order to screen out  
222 unreliable interpretations. This problem applies to the specimen level (which statistics  
223 and what threshold values to use?, e.g. Paterson et al., 2014) as well as to the sample/site  
224 level (how many specimens should be averaged? and how to account for internal  
225 consistency?, e.g. Paterson et al., 2010). Given the complexity of the raw experimental  
226 data the differences between different interpretations made using different acceptance  
227 criteria may be significantly large. Another key problem is that the reported error  
228 estimation of the sample/site mean (in the form of one standard deviation) does not  
229 account for the entire sources of uncertainty at the specimen level interpretation.

230 In this work we employ a different technique for interpreting the data. We apply the  
231 automatic interpretation available via the Pmagy Thellier-Gui (described in detail in  
232 Shaar and Tauxe, 2013). The main features of the automatic interpretation technique are  
233 the ability to guarantee consistency, objectivity, and reproducibility of the interpretations.

234 To use the automatic interpretation technique the user first has to choose acceptance  
235 criteria (from the list given in Paterson et al, 2014; <http://www.paleomag.net/SPD/>). Then  
236 the program performs the following tasks:

- 237 1) The program analyzes all the possible best-fit lines of each Arai plot separately  
238 and isolates the interpretations that pass the specimen selection criteria.

- 239 2) Each interpretation is corrected for the effect of anisotropy, cooling rate (for slow-  
240 cooled samples such as pottery), and if needed, non-linear-TRM (NLT) (e.g., Figs  
241 S3,S4, Supplementary Material).
- 242 3) The program calculates all the possible sample/site means and isolates all the  
243 means that pass the sample/site acceptance criteria.
- 244 4) From all the sample/site means that pass criteria: the ‘most likely’ mean is the one  
245 that has the lowest standard deviation (best agreement within a cooling unit or  
246 site). The uncertainty bound of the ‘most likely’ mean is the standard deviation.
- 247 5) The ‘extended’ uncertainty bounds of the sample/site paleointensity are calculated  
248 by finding from all the means that passed the criteria two end-case interpretations:  
249 the lowest ( $B_{\min} \pm \sigma_{\min}$ ) and the highest ( $B_{\max} \pm \sigma_{\max}$ ). The ‘extended’ uncertainty  
250 bounds are [ $B_{\min} - \sigma_{\min}, B_{\max} + \sigma_{\max}$ ]. This ‘extended’ error envelope is  
251 significantly larger than what is conventionally reported as uncertainty ( $1\sigma$ ).  
252 Nevertheless, we believe that this calculation is more robust and consistent than  
253 the conventional approach because it takes into consideration all the possible  
254 interpretation at the specimen level that pass the criteria, and not just a collection  
255 of subjective interpretations chosen by the analyst.

256 All the measurement data and the software to analyze it (PmagPy ThellierGui) are  
257 accessible from the MagIC database (<http://earthref.org/MAGIC/>) and from the PmagPy  
258 homepage (<http://earthref.org/PmagPy/cookbook/>) respectively. This gives other  
259 researchers full access to the raw data, and allows others to reproduce our final  
260 interpretations and re-interpret them using any given set of acceptance criteria, if they so  
261 choose.

### 262 Specimen paleointensity statistics

263 The success of the automatic interpretation procedure depends on the assumption that the  
264 acceptance criteria successfully screen out unreliable interpretations. The set of statistics  
265 we use follows Shaar and Tauxe (2013) who argue that the use of seven statistics, as  
266 listed below, covers the most common causes for failure of a paleointensity experiment  
267 (for a detailed definition of the statistics see <http://www.paleomag.net/SPD/> - Paterson et  
268 al., 2014).

269 Figure 4a shows nearly ideal experimental results with a straight-line Arai plot,  
270 successful pTRM checks and a straight Zijdeveld plot converging to the origin. In this  
271 case, different choices of temperature bounds would yield nearly identical slopes  
272 resulting in the same paleointensity estimates. Clearly, interpretations based on such data  
273 should pass the selection criteria. Figs. 4b-f show examples of lower quality of  
274 Arai/Zijdeveld plots rejected by our selection criteria. In these cases, different choices of  
275 temperature bounds yield significantly different slopes. Choosing the most appropriate  
276 slope is somewhat arbitrary. Moreover, it is clear that these specimens do not fulfill the  
277 basic assumption underlying the Thellier method (pure TRM carried exclusively by no-  
278 interacting single domain that do not alter during the experiment) and thus the reliability  
279 of these interpretations is questionable.

280 The specimen criteria we use are as follows:

- 281 •  $FRAC$  (Shaar and Tauxe, 2013)  $\geq 0.79$ .  $FRAC$  is a remanence fraction statistic  
282 calculated by the vector difference sum ( $VDS$ , Tauxe and Staudigel, 2004) of the  
283 selected component divided by the total  $VDS$ . A low  $FRAC$  indicates that only a small  
284 fraction of the remanence is used for paleointensity estimation (e.g. Fig. 4b).  $FRAC$  is  
285 more suitable for general use than  $f$  (Coe et al., 1978) and  $f_{vds}$  (Tauxe and Staudigel,  
286 2004), as  $f$  and  $f_{vds}$  might lead to misleading high or low values, respectively, for some  
287 non-ideal Arai plots (e.g. Fig. 2 in Shaar and Tauxe, 2013; Fig. 4b).
- 288 •  $\beta$  (Coe et al., 1978; Selkin and Tauxe, 2000)  $\leq 0.1$ .  $\beta$  is the standard error of the least  
289 square line slope of the selected segment in the Arai plot divided by the slope. A high  
290  $\beta$  value indicates a nonlinear or highly scattered Arai plot (but low  $\beta$  does not always  
291 guarantee a straight line, e.g. Fig. 4c).
- 292 •  $SCAT$  (Shaar and Tauxe, 2013): A Boolean scatter statistic relying on  $\beta$ .  $SCAT$  is  
293 determined by a polygon (dashed lines in Fig. 4) drawn on the Arai plot using the  
294 threshold value of  $\beta$ .  $SCAT$  is True (pass) only if all the data points including the  
295 pTRM checks fall inside the polygon. A False (fail) value can result from non-  
296 reproducible pTRM checks, zigzagged, scattered or non-linear Arai plot, or a poorly  
297 defined best-fit line (e.g. Fig. 4c).

- 298 •  $N_{pTRM} \geq 2$ : the number of pTRM checks carried out before reaching the highest  
299 temperature in the selected segment. Fewer checks indicate that alteration was not  
300 properly tested.
- 301 •  $GAP-MAX$  (Shaar and Tauxe, 2013)  $\geq 0.5$ : Maximum Gap Statistic. The longest  
302 vector difference between consecutive data points in the selected segment of the Arai  
303 plot, normalized by the VDS of the selected segment. A high  $GAP-MAX$  indicates a  
304 poorly defined Arai plot with two data points separated by a large gap (e.g. Fig. 4d).
- 305 •  $MAD$  (Kirschvink, 1980)  $\leq 5$ : Free floating maximum Angular Deviation of the  
306 principle component best fit line of the Zijderveld plot. A high  $MAD$  indicates a non-  
307 linear or scattered Zijderveld plot (e.g. Fig. 4e).
- 308 •  $DANG$  (Tauxe and Staudigel, 2004)  $\leq 10$ : The deviation angle of the Zijderveld best-  
309 fit line from the origin. A high value indicates that the Zijderveld plot does not  
310 converge to the origin (e.g. Fig. 4f).

311 In addition to the above, alteration during the ATRM and NLT procedures is calculated  
312 by comparing the first and the last measurements. Alteration is calculated in the ATRM  
313 procedure by comparing the following three pairs of measurements (after baseline  
314 subtraction): +x and -x, +y and -y, +z and -z. The threshold value for the alteration check  
315 is 5%.

### 316 Sample paleointensity statistics

317 At the sample level (sample = cooling rate unit) we use the following statistics as  
318 acceptance criteria:

- 319 •  $N_{sample} \geq 3$ : minimum specimens required for samples mean calculation.
- 320 •  $\sigma (\mu T) \leq 3 \mu T$  : standard deviation of the sample mean in unit of  $\mu T$ .
- 321 •  $\sigma (\%) \leq 8 \%$ : standard deviation of the sample mean divided by the mean in units of  
322 %.

323 The last two statistics are combined with a logical 'or' function, i.e  $\sigma$  passes the criteria if  
324  $\sigma \leq 3 \mu T$  or  $\sigma (\%) \leq 8 \%$

325 In addition, specimens that failed the anisotropy procedure (e.g. due to alteration), and  
326 specimens that were not corrected for anisotropy because specimens fell apart from the  
327 glass tube, were excluded from sample mean calculation.



328 **2.5 Hysteresis and FORCs**

329 To better understand the rock magnetic characteristics of the slag material we measured  
330 hysteresis loops of one specimen from each sample that passed the final acceptance  
331 criteria. In addition, we collected first order reversal curves (FORC, Pike et al., 1999)  
332 from six specimens – three from each mound. Hysteresis and FORCs were collected  
333 using a Princeton Measurements Vibrating Sample Magnetometer ( $\mu$ VSM) at the  
334 Institute of Rock Magnetism (*IRM*), University of Minnesota. Hysteresis data were  
335 analyzed via PmagPy software package (Tauxe, 2010). FORCs were analyzed using  
336 FORCinel software (Harrison and Feinberg, 2008).

337

338 **2.6 Electron microscopy**

339 To identify the ferromagnetic phase carrying the ancient TRM we conducted electron  
340 microscopy analyses of selected slag specimens that passed the acceptance criteria.  
341 Specimens were embedded within phenolic resin and polished to 25 nm using colloidal  
342 silica for scanning electron microscope imaging and elemental analyses. Crystallographic  
343 information on the silicate and oxide mineralogy within the slag samples was obtained  
344 from polished sections using a JEOL 6500 field emission gun (FEG-SEM) outfitted with  
345 an HKL electron backscatter diffraction (EBSD) detector at the University of Minnesota.  
346 EBSD measurements were conducted using an operating voltage of 20 kV and a working  
347 distance of 25 mm. Minerals were identified by indexing diffraction patterns using  
348 Channel 5 software. Crystallographic solutions were accepted only if the mean angular  
349 deviation (MAD) value was less than  $1.4^\circ$ . Measurements of elemental abundances were  
350 collected using an accelerating voltage of 15 kV and a working distance of 10.0 mm.  
351 Spot energy dispersive spectroscopy (EDS) measurements were collected using a  
352 Thermo-Noran Vantage System. The diameter of the interaction volume for elemental  
353 measurements was  $\sim 2.5 \mu\text{m}$  in silicate minerals and  $\sim 2.0 \mu\text{m}$  in oxide and sulfide  
354 minerals. Matrix correction coefficients (Z, A, and F) were calculated using the  
355 Phi(Rho\*z) method of Pouchou & Pichoir (1984) and Bastin & Heijligers (1991). X-ray  
356 spectra were collected using counting times of 60 seconds and a probe current of 100 nA.

357

358 **3 Results**

359 **3.1 Radiocarbon results and age-height modech**

360 The chronological models are constructed using Bayesian analysis, which combines *prior*  
361 information (stratigraphic order of the samples and their relative heights) with *likelihood*  
362 information (absolute radiocarbon dates). The analysis is done via the Oxcal program  
363 (Ramsey, 2009). The Oxcal input programs, the radiocarbon dates, and the Oxcal output  
364 table are listed in an Excel file in the Supplementary Material.

365 SU1

366 The prior information in SU1 is the relative heights of the samples measured by the Total  
367 Station. **As do** not have any prior information on the deposition rate, we assume **a random**  
368 **deposition** rate. This is done using the P\_Sequence procedure in Oxcal (Remsey, 2008).

369 In addition, as we don't know the increments of the chronological pieces we follow  
370 Ramsey and Lee (2013) and simulate different age-depth models using a range of  
371 increments from 1mm to 1m. The final age-height model is the average of all the  
372 simulated models. To test the Poisson height-depth model we ran a "Sequence" model  
373 that uses the stratigraphic order of the samples as **prior** and ignores their heights. The  
374 Sequence model is more flexible than the P\_Sequence model, but it cannot be used to  
375 model the height-age relation.

376 An initial P\_Sequence analysis of the calibrated radiocarbon ages of SU1 shows that in  
377 general, the sample age increases with depth, such that the oldest samples are at the  
378 bottom of the mound. Some shifts from the general age-depth trend are seen, but these  
379 are expected because of specific uncertainties in the chronological analysis that cannot be  
380 completely eliminated, such as the time gap between the age of the stem when it was cut  
381 and the time when it was used and dumped in the mound (the "Old Wood Effect",  
382 important especially when the outermost ring is unidentifiable). The agreement index (the  
383 overlap of the posterior probability and the likelihood probability distributions) of the  
384 initial P\_sequence model is lower than is normally considered acceptable  $A_{\text{model}} = 40\% <$   
385  $60\%$  due to an exceptionally low agreement index (3.1%) of sample su1094. If we  
386 discard the outlier sample su1094 we get  $A_{\text{model}}=146$  and sample agreement indices well  
387 above acceptable values. The age model discarding sample su1094 is shown in Figure 5b.

388 The P\_sequence procedure yields a height-age model with likelihood probability  
389 distributions for each height in the mound. The height-age model is used to assign an age  
390 distribution for each of the slag samples. The age constraints for the bottom and the top  
391 of the mound are: 1) Bottom: 68.2% probability range = 362 to 404 CE, 95.4%  
392 probability range = 321 to 416 CE, median=380, 2) Top: 68.2% probability range = 403  
393 to 440 CE, 95.4% probability range = 397 to 531 CE, median=426. These distributions  
394 suggest that the mound was accumulated in a period of about 46 years (difference  
395 between the medians), with 68.2% probability range of 78 years, and 95.4% probability  
396 range of 210 years.

### 397 MK1

398 There are three main difficulties in dating the MK1 mound. (1) Identifying the wood  
399 species and isolating the outermost rings was hard because the charcoal is poorly  
400 preserved, consisting of mostly small fragments, and there are fewer samples with  
401 preserved bark and/or outer rings. (2) The dates are located within the so-called “Iron  
402 Age plateau” in the  $^{14}\text{C}$  calibration curve (Fig. S5, Supplementary Material), resulting in  
403 a large dating uncertainty. (3) There is no consistent age-height correlation between the  
404  $^{14}\text{C}$  age and stratigraphic level throughout the mound (unlike in SU1, see Fig. 5).  
405 Therefore, we model the  $^{14}\text{C}$  dates in MK1 as a single Phase in OxCal program. This  
406 model does not assume any correlation between charcoal age and depth.

407 **Fig. 5c** shows the likelihood functions of the calibrated ages from MK1 ordered  
408 according to their stratigraphic position in the mound. We recall that the quality of the  
409 charcoals from MK1 is significantly lower than in SU1. The ages of six samples overlap  
410 and their ages range from the 8<sup>th</sup> to the beginning of the 4<sup>th</sup> centuries BCE. Two other  
411 samples have ages that differ from the unmodeled date ranges: charcoal fragment  
412 mk1L.5, which was sampled from flotation and has an older age range, and sample  
413 mk1083, which is younger than the other samples. It is possible that there is some mixing  
414 of fine materials within the mound, which might introduce younger material (like  
415 mk1083) into an older context (or vice versa). Small charcoal fragments (like mk1L.5,  
416 which is only 1mm) can be especially mobile. It is also possible that mk1L.5 is older

417 because of old wood bias, since it is not known if the sample is part of the outermost part  
418 of a branch/twig.

419 In MK1 we do not use the stratigraphic order of the radiocarbon dates in the age  
420 modeling. Instead, we group all the eight samples as one phase. The supplemental Excel  
421 file lists Oxcal output for three different models. ‘Model 1’ uses all the ages, ‘Model 2’  
422 discards sample mk1083, and ‘Model 3’ discards samples mk1083 and mk1L.5. ‘Model  
423 3’ is our preferred model as it excludes dates that are likely unreliable. We use the  
424 resulting age model to assign an age to each layer (locus) by evenly distributing the  
425 difference between the modeled likelihood distributions of the top and the bottom of the  
426 mound among the slag layers. This age model assumes a constant deposition rate, and  
427 helps putting the paleointensity results in a chronological reference frame. However, we  
428 note the large uncertainty in this age model.

### 429 **3.2 Paleointensity**

430 The strict specimen acceptance criteria listed in Section 2.4 were chosen to screen out  
431 unreliable behavior in the paleointensity experiments exemplified by non-linear Arai  
432 plots, unreproducible pTRM checks, curved or diverging Zijdeveld plots, and poorly  
433 determined anisotropy tensors. A total of 267 specimens (out of 673) passed specimen  
434 acceptance criteria. This low, but reasonable rate of success (40%) reflects the difficulty  
435 in isolating specimens with high quality behavior such as in Fig. 4a. Figure S6,  
436 Supplementary Material, displays a histogram showing the distribution of the anisotropy  
437 degree ( $P=\tau_1/\tau_2$ ) of the specimens that passed the selection criteria, demonstrating that  
438 most of the specimens exhibit relatively high P values. For this reason, we discard  
439 specimens that failed the anisotropy experimental procedures from sample mean  
440 calculations (e.g., alteration observed during the ATRM procedure, or because the glue  
441 holding the specimen in the vial got loose during the anisotropy experiment at high  
442 temperature). Figure S6 shows histograms of the NLT correction. Except for a few cases,  
443 the NLT correction was less than 4% suggesting that NLT effect is insignificant.

444 With no criteria at the sample level that test the internal consistency in the cooling unit  
445 we get 40 samples that have at least 3 successful specimens. Yet, the overall data exhibit  
446 significant discrepancies (Figure S9, Supplementary Material). To screen out the noisy

447 data we apply the criteria at the sample level ( $\sigma \leq 3 \mu\text{T}$  or  $\sigma\% \leq 8 \%$ ) and get 22  
448 successful samples that passed the criteria.

449 The overall low success rate (22 samples out of 153 analyzed) and the difficulty in  
450 isolating well-behaved specimens suggests that, in general, the Cypriot copper slag may  
451 not be an ideal paleomagnetic recorder. Yet, in this work we demonstrate that with  
452 sufficient laboratory effort and strict choice of selection criteria at the specimen and  
453 sample level, a useful number of robust paleointensity estimates can be obtained.

454 Table 1 lists the final paleointensity estimates of the samples. The STDEV-OPT mean is  
455 the mean that has minimum standard deviation, the STDEV-OPT sigma is the standard  
456 deviation of the mean (the conventional estimate for error bounds in paleointensity  
457 studies), and the ‘extended error bound’ is the maximum /minimum means the passed the  
458 criteria +/- their standard deviations (see Section 2.4 for details). We treat STDEV-OPT  
459 mean as the ‘most likely’ result as it reflects the best internal consistency within the  
460 cooling unit, but prefer the larger ‘extended error bound’ as our error estimation. All  
461 samples are slag material except su102501 (baked clay).

462 Figure 6a,b show the paleointensity time series from SU1 plotted versus height (a) and  
463 versus age (b). Horizontal error-bars in Figure 6b show the 68.2% probability range of  
464 the modeled ages. Blue (short) y-errorbars are the standard deviation, and the red (long)  
465 errorbars are the STDEV-OPT extended error bounds. The extended errorbars of the SU1  
466 data (red) are mostly overlapping. However, the SU1 data suggest an interesting steady  
467 decrease in field intensity during in upper part of the mound. This behavior is discussed  
468 in details in Section 4.1.

469 Figure 6c show paleointensity time series from MK1 plotted versus age, where the large  
470 horizontal (age) error bars are not displayed for clarity. The data from MK1 data  
471 demonstrate excellent agreement between samples collected from the same loci, i.e.  
472 samples that are expected to yield similar paleointensity results. All the extended  
473 errorbars (red), except one (sample mk100702) overlap suggesting that any changes in  
474 the geomagnetic field intensity were small and undetectable.

475 Figure 6d shows the new data from this study with previously published data from Israel  
476 and Syria (Ben-Yosef et al., 2008; Genevey et al., 2003; Gallet et al., 2006). The

477 agreement between the averaged values in MK1 and SU1 and the contemporaneous  
478 average values from Syria is excellent.

479 A MagIC Project folder that includes formatted files with the raw data, the paleointensity  
480 interpretations, and the acceptance criteria, can be downloaded from the MagIC database  
481 (<http://www.earthref.org/MAGIC/>).

### 482 **3.3 Hysteresis and FORC**

483 Figure S7, supplementary material show Day diagram (Day et al., 1977) and squareness  
484 versus coercivity plot (Tauxe et al., 2002) of the specimens that were selected for  
485 hysteresis analysis. The hysteresis parameters fall in the PSD region and may represent a  
486 mixture of different domain states (Dunlop et al., 2002). In general, specimens from MK1  
487 and from SU1 are grouped in different fields in the diagrams, where specimens from SU1  
488 fall closer to the ideal SD region and have higher coercivities. The FORC diagrams  
489 shown in Figure 7 (See also Figure S8, Supplementary Material) indicate that slags from  
490 both mounds exhibit a mixture of two populations: MD, which dominates the lower  
491 coercivity spectrum ( $H_c \leq 10$  mT) and small PSD to SD with symmetric coercivity  
492 distributions about the  $H_u$  axis that extend as high as 200 mT (Fig, 7c). The median of  
493 the coercivity distributions range from 25 to 50 mT for the SU1 specimens, and from 15  
494 to 30 mT for the MK1 specimens. The FORC analyses indicate that glassy slag material  
495 can contain a large population of high coercivity SD-like particles, which may act as  
496 ideal paleointensity recorders. Yet, as noted earlier, isolating this “SD” part of the slag  
497 while excluding the multidomain component is a challenging task with low rate of  
498 success.

### 499 **3.4 Electron microscopy**

500 Representative SEM images of SU and MK slags are shown in Figure 8 and capture a  
501 sense of the wide variations in mineralogy, grain size and shape, and crystallization order  
502 that can occur in metallurgical slags. The general mineralogy of all of the slag samples  
503 can be divided into four categories: Cu-rich sulfide grains (sometimes rich in Fe), silicate  
504 minerals, oxide minerals, and silicate glass, which tends to serve as the matrix for the  
505 slag.

506 Cu-rich sulfide minerals, often with high concentrations of Fe, were observed in all  
507 samples in varying concentrations. Grain sizes were often smaller than the interaction  
508 volume of the electron beam, preventing unambiguous elemental measurements, although  
509 EBSD patterns indicate that sulfides with cubic, monoclinic, and hexagonal crystal  
510 symmetries are present. Grain boundaries were typically well-rounded (droplet-like) and  
511 many grains displayed internal structure suggestive of intergrowths between multiple  
512 sulfide phases. Many Cu-Fe-S minerals are known to alter to magnetite during heating,  
513 especially between temperatures of 300 and 450°C. Such alteration can often cause  
514 paleointensity experiments to fail, as the new magnetite will cause a specimen to acquire  
515 an anomalously high remanence during pTRM steps.

516 The particular silicate assemblage present in a slag specimen is a reflection of the  
517 composition of the ores that were employed in smelting, the cooling rate, and oxygen  
518 fugacity of the silicate melt. As such, a diversity of silicate phases and textures were  
519 observed in specimens from SU1 and MK1. Olivine was the most frequently occurring  
520 silicate mineral, and although no end-member compositions were observed, olivine  
521 compositions ranged from fayalitic (Fig 8a,c-f) to forsteritic (Fig.8b), and in one instance  
522 kirschsteinite ( $\text{CaFeSiO}_4$ ) was observed (Fig. 8f). Although there is a solid solution  
523 between fayalite and kirschsteinite, occurrences of the latter are rare in nature and are  
524 typically restricted to Ca-Fe-rich silicate melts that are silica-undersaturated and allowed  
525 to cool in low-pressure conditions. This is exactly the environment that exists for most  
526 metallurgical slags, where kirschsteinite can be common (Wyderko and Mazanek, 1968).  
527 Olivine grains generally occur as large skeletal laths that confine the sizes and shapes of  
528 other minerals in the slag, an indication that they nucleated from the melt first and grew  
529 fastest (Fig. 8a, c, f). Other silicates include anorthite ( $\text{CaAl}_2\text{Si}_2\text{O}_8$ ) (Fig. 8b) and melilite,  
530  $(\text{Ca,Na})_2(\text{Al,Mg,Fe}^{2+})[(\text{Al,Si})\text{SiO}_7]$  (Fig. 8d), which occurs naturally in metamorphosed  
531 limestones, in modern industrial slags (e.g., Broadbent, 1987; Min'ko et al., 1988) as well  
532 as in archaeological slags (e.g., Manasse and Mellini, 2002).

533 Nearly pure magnetite is the most common oxide present in the slags from both SU and  
534 MK. Minor substitution of Ti, Mg, and Al may be possible in some instances, but is  
535 difficult to conclusively demonstrate owing to the extraordinarily fine scale of the  
536 dendrites relative to the interaction volume of the electron beam. Grains are usually

537 dendritic with branches that extend for several micrometers and end as nanometer-scale  
538 branch tips. Such fine-scale dendritic structures have been shown previously to produce  
539 SD-like behavior (Shaar and Feinberg, 2013). The dendrites show 2- and 3-fold  
540 symmetry, index as cubic, and are slightly smaller in scale in samples from the SU  
541 mound. In several instances it is clear that the magnetite dendrites are nucleating in a  
542 crystallographically-controlled manner from the edge of a nearby large silicate  
543 phenocryst (e.g., Fig. 8c). This kind of topotactic growth is common in rapidly cooling  
544 systems and may provide some explanation for the exceptional remanence anisotropy  
545 observed in some samples. In the one instance, titanomagnetite occurs as aggregates of  
546 nanometer-scale grains clustered between laths of anorthitic plagioclase rather than as  
547 dendrites (Fig. 8b). Fe-bearing spinel also occurs in a more limited extent in some of the  
548 MK samples.

549 The internal textures of the slag specimens may also provide information about why  
550 some specimens fail during paleointensity experiments. Some samples display large  
551 silicate xenocrysts, indicating that certain silicate minerals were not completely melted  
552 during the smelting process. Others showed brecciated textures infilled by silicate glass  
553 (e.g., SU-109001e). Another specimen (MK-107901f) displayed internal quenching  
554 surfaces (Fig. 8e) indicating that the specimen is actually a glass agglutinate, where  
555 molten glass was deposited onto a previously cooled surface. In the case of brecciated  
556 and agglutinated slags, there is the possibility that more than one component of  
557 thermoremanence may be retained within a single specimen. Such multicomponent  
558 demagnetization curves have the potential to create large MAD values, exceeding the  
559 threshold quality control criteria, causing a paleointensity experiment to fail (e.g., Fig.  
560 4e).

## 561 **4 Discussion**

### 562 **4.1 Decadal rates of change in geomagnetic field intensity**

563 The main objective of this study is to document any sub-century scale variations in the  
564 intensity of the ancient field recorded in the Cypriot slag mounds. We investigate two  
565 slag mounds – MK1 (7<sup>th</sup> to 5<sup>th</sup> centuries BCE) and SU1 (4<sup>th</sup> to 5<sup>th</sup> century CE). MK1  
566 yielded 12 reliable paleointensity means that passed our strict selection criteria (Table 1).



567 All the samples in MK1, except one, have overlapping extended error bounds (red bars in  
568 Fig. 6), and therefore, we consider them to be statistically indistinguishable. We recall  
569 that the chronology of MK1 could not be precisely estimated because of the quality of the  
570 charcoals and the “Iron Age plateau” in the  $^{14}\text{C}$  calibration curve (Section 3.1).

571 Regardless the difficulty in establishing the exact chronology of MK1, most of the MK1  
572 time series indicates a relatively smooth behavior of the field with no substantial changes  
573 in field intensity that could be detected by the paleointensity procedure.

574 In contrast to MK1, the SU1 data suggest a changing geomagnetic field. Figure 6b show  
575 an increase in field intensity until a peak value around ca. 400 – ca. 410 CE (samples  
576 su101801 to su110801) followed by a steady decrease. The slope of this line, calculated  
577 by a y-error weighted (red error bars) least squares line over eight samples from  
578 su101801 onward is shown as a green dashed line in Fig. 6b.

579 We try to put some constraints for the rate of the decrease shown in figure 6b using a  
580 bootstrap analysis on eight samples from su101801 onward. In each bootstrap iteration an  
581 x-axis value is drawn from each sample (N-1 samples) assuming a normal age  
582 distribution (using the  $\nu, \sigma$  of the height-age model), and a y-axis value is drawn  
583 assuming a uniform distribution within the ‘extended error bounds’ (the red errorbars in  
584 Figure 6). As the age distribution overlap, the stratigraphic order of the samples is forced.  
585 In each bootstrap iteration we calculate the slope of the best fit line (nT/year), and the

586 relative change in terms of % change  $(100 \cdot \frac{B_{\max} - B_{\min}}{\text{mean}(B_{\max}, B_{\min})})$ . The latter calculation is

587 done in order to be able to compare rates of changes for different absolute field  
588 intensities. The bootstrap distribution of the rate (nT/year) is shown in Figure 6e. The  
589 bootstrap distribution of the relative change per decade (%/decade) is shown in Figure 6f.

#### 590 **4.2 Comparison with the historically measured geomagnetic field**

591 The data from the Cypriot slag mound, especially the rapid decay shown in SU1, should  
592 be discussed in the context of high precision human measurements of the geomagnetic  
593 field. The first measurement of field intensity was conducted by Carl Friedrich Gauss in  
594 1832 (Malin and Barraclough, 1982). Continuous measurements ever since allow  
595 spherical harmonic modeling of the field (e.g. Jackson et al., 2000; Finlay et al., 2010)

596 and evaluation of the geomagnetic secular variation (SV) at any point on Earth. Here, we  
597 use the gufm1 model (Jackson et al., 2000) from 1840 to 1990 and the IGRF models from  
598 1990 to 2010 (Finlay et al., 2010) to calculate the relative % change (

599  $100 \cdot \frac{B_{\max} - B_{\min}}{\text{mean}(B_{\max}, B_{\min})}$ ) of the geomagnetic field intensity on Earth's surface during the

600 past 170 years (referred to as “the historical field” hereafter). Figs. 9a,b display global  
601 maps of the maximum change per decade (Fig. 9a) and per century (Fig. 9b) . The maps  
602 show that the relative change on most of Earth's surface did not exceed 2.0 % per decade,  
603 and that most of the high temporal variability was concentrated in three confined lobes in  
604 the southern hemisphere: southeast and southwest of South Africa, and in South America.  
605 These lobes, when projected on Earth's core-mantle boundary are interpreted as dynamic  
606 flux patches, and it is their growth, migration, and expansion that produces the short term  
607 variations observed on Earth's surface (Gubbins, 1987, Jackson et al., 2000, Hulot et al.,  
608 2002, Gubbins et al., 2006, Olson and Amit, 2006). Interestingly, two of the active lobes  
609 in the southern hemisphere are paired with less active lobes at roughly the same longitude  
610 in the northern hemisphere: in the western Atlantic and the Middle East (our study area,  
611 which is marked with a triangle). The lobes with the highest rates of change in the  
612 historical field are marked with stars in Figs. 9a,b. The intensity curves at the location  
613 marked with stars are shown in red in Fig. 9c.

614 The archaeomagnetic data shown in Fig. 6 have sufficient resolution to enable  
615 contextualization of the rates of change shown in Fig. 9. We use the new data to address  
616 the question of whether the rates in the historical field represent typical characteristics of  
617 secular variation or, instead, indicate unusual behavior attributable to extreme events  
618 such as an imminent reversal as suggested by some researchers (e.g. Olson, 2002). Our  
619 new data show that it is likely that relative change in Cyprus during the 5<sup>th</sup> century CE  
620 was of the order of the highest relative change in the historical field observed anywhere  
621 on Earth. In view of the new data and in agreement with recently published  
622 archaeomagnetic data (see below), the rapid intensity changes in the historical field  
623 should be interpreted as a normal phenomenon rather than an exceptional one.

624 This study complements recent archaeomagnetic studies that have suggested high  
625 temporal variability in the ancient field. Gallet et al. (2003) identified “archaeomagnetic

626 jerks”, short intervals of rapid changes in the direction of the field associated with  
627 intensity maxima apparent in the archaeomagnetic records of Europe and the Middle  
628 East. Ben-Yosef et al. (2009) and Shaar et al. (2011) reported short-lived high field  
629 anomalies during the Middle East Iron Age, referred to as “geomagnetic spikes”. Other  
630 episodes with fast intensity changes of about 40% per century were reported in  
631 archaeointensity records from Western Europe (Genevey et al., 2009; Gomez-Paccard et  
632 al., 2012) and Eastern Europe (Kovacheva et al., 2009). Thus, there is increasing  
633 evidence for high temporal variability in the ancient geomagnetic field. However, owing  
634 to the limited dating precision of most of the materials in the archaeomagnetic record  
635 (mostly of potsherds, baked clays, and volcanic rocks) and other sources of experimental  
636 uncertainties such as cooling rate effect in pottery (e.g. Genevey et al., 2008) sub-century  
637 scale variations are inherently smoothed out in the compilation process of conventional  
638 archaeomagnetic datasets. Sub-century scale variation that might be obscured in the  
639 available paleomagnetic records can be recovered using stratigraphically ordered high  
640 accumulation rate slag mounds, such as the ones studied here.

#### 641 **4.3 The Middle Eastern geomagnetic active lobe**

642 One interesting observation from Figure 9 is that significant changes in the geomagnetic  
643 field intensity do not occur randomly, and are instead concentrated in preferred locations.  
644 Assuming that the configuration of the geomagnetic field has not fundamentally changed  
645 over the past two millennia, we suggest that the rapid temporal variation observed in our  
646 study area (here, and in Ben-Yosef et al., 2009 and Shaar et al., 2011) is not coincidental.  
647 We suggest that the Middle Eastern area (triangle in Figure 9a) is the northern  
648 hemisphere mirror image of the presently active region south of Africa (star in Figures  
649 9a). Together, the two areas may represent a closely related columnar convection  
650 structure. We conclude that at least one difference between the historical and the more  
651 ancient field is the level of activity in the northern hemisphere, which has been  
652 suppressed during the past centuries, but was significantly higher in the past.

### 653 **5 Summary**

- 654 • We investigate two stratified slag mounds in Cyprus - SU1 (4<sup>th</sup> -5<sup>th</sup> century CE, 25  
655 meter in height) and MK1 (7<sup>th</sup> -5<sup>th</sup> century BCE, eight meter in height) in order to

656 construct two sub-century scale paleointensity time series. The chronology of SU1  
657 mound is modeled by ten radiocarbon dates of short-lived organic materials extracted  
658 from identified outer rings of small branches and twigs. The chronology of MK1 is  
659 modeled by six radiocarbon dates of charcoals with less quality. Absolute  
660 paleointensity estimates are obtained from Thellier type IZZI experiments with  
661 anisotropy and non-linear TRM assessments on geo-referenced slag samples collected  
662 from different horizons in the mounds.

- 663 • We employ here a recently published technique for automatic interpretation of  
664 paleointensity data. The automatic procedure is designed to minimize user-biased  
665 uncertainties attributed to subjective manual interpretation. The automatic procedure  
666 provides a larger, but more robust error estimation, and ensures consistency and  
667 reproducibility.
- 668 • In general, the Cypriot slag material behaved poorly in the paleointensity experiments  
669 and we reject more than 60% of the specimens analyzed based on low quality Arai  
670 and Zijdeveld plots. In addition, as the slag is very anisotropic, we reject specimens  
671 that failed the anisotropy correction procedure. Specimens that passed the strict  
672 paleointensity screening process demonstrated SD-like behavior in the paleointensity  
673 experiments, and had narrow high coercivity SD pattern in FORC analysis.
- 674 • Electron microscopy indicates that primary remanence carrier is nearly pure dendritic  
675 magnetite. The crystallographically-controlled nature of the dendrites, combined with  
676 topotactic nucleation along large laths of olivine give rise to the slag's high degree of  
677 remanence anisotropy. A portion of the slag samples show brecciated and  
678 agglutinated textures, raising the possibility that multiple components of  
679 thermoremanence maybe retained within a single specimen. Such samples are  
680 expected to fail the MAD/DANG criteria in the paleointensity experiments.
- 681 • Ten paleointensity estimates from MK1 yield indistinguishable results suggesting that  
682 the field during the time MK1 accumulated was stable with no dramatic changes.
- 683 • Ten paleointensity estimates from SU1 suggest a drop in field intensity during the 5<sup>th</sup>  
684 century CE. The relative change was likely to be more than 2% per decade.
- 685 • We analyze the relative decadal change on Earth's surface during the past 170 years  
686 using the gufm1 and IGRF models, and find that high relative change between 2.5 to

687 4.8% per decade occurred only in few confined locations: Central and South America,  
688 southern Atlantic, and South Africa. In most of Earth surface the relative change did  
689 not exceed 2% per decade.

- 690 • We suggest that the rapid temporal variation observed in our study area (here and in  
691 Ben-Yosef et al., 2009 and Shaar et al., 2011) is related to a Middle Eastern “activity  
692 lobe” - the northern hemispheric mirror image of the presently highly active region  
693 south of Africa. Together, this pair may represent a geomagnetic expression of a  
694 columnar convection structure within the liquid iron outer core.
- 695 • The entire measurement data, the final interpretations, and the software to analyze the  
696 data (PmagPy Thellier GUI) are accessible from the MagIC database  
697 (<http://earthref.org/MAGIC/>) and from the PmagPy homepage  
698 (<http://earthref.org/PmagPy/cookbook>).

699

700

## 701 **Acknowledgments**

702 The authors wish to thank Mr. Constantinos Xydas, CEO of Hellenic Copper Mines Ltd.,  
703 for his invaluable assistance during the excavations at Skouriotissa mines. We  
704 acknowledge the help of Matthew Vincent and Ashley Richter from Calit2, UCSD who  
705 operated the Total Station. We wish to thank the volunteers of the field expedition: Uri  
706 Davidovich, Jorge Perez, Philip Staudigel, Jennifer Roebber, and Alina Levy. We would  
707 like to thank Cathy Constable, Jeff Gee, Sanja Panovska and Geoff Cromwell for  
708 constructive comments and suggestions. Jason Steindorf made most of the paleomagnetic  
709 measurements for this study. This work was funded by NSF grants EAR 0944137 to LT  
710 and TEL and **EAR 1141840 to LT**. We thank Pierrick Roperch and an anonymous  
711 reviewer for thorough reviews of an earlier version of the manuscript that significantly  
712 improved the current manuscript. Parts of this work were carried out in the  
713 Characterization Facility, University of Minnesota, which receives partial support from  
714 NSF through the MRSEC program.

715

716 The authors dedicate this article to the memory of Hagai Ron, teacher, colleague, and  
717 friend.

718

719 **References**

720 Akkemik, Ü., Yaman, B. (2012), Wood Anatomy of Eastern Mediterranean Species.  
721 Remagen-Oberwinter : Kessel Publishing House.

722 Barraclough, D.R., Carrigan, J.G., Malin, S.R.C. (2000), Observed geomagnetic field  
723 intensity in London since 1820. *Geophys. J. Int.* 141, 83-99. doi: 10.1046/j.1365-  
724 246X.2000.00062.x

725 Bastin, G. F., and Heijligers, H. J. M. (1991), Quantitative electron probe microanalysis  
726 of ultra-light elements (boron-oxygen), in *Electron probe quantitation*, K. J. F. Heinrich  
727 and D. E. Newbury eds., Plenum, New York, 145-161.

728 Ben-Yosef, E., Ron, H., Tauxe, L., Agnon, A., Genevey, A., Levy, T.E., Avner, U.,  
729 Najjar, M. (2008), Application of copper slag in geomagnetic archaeointensity research.  
730 *J. Geophys. Res.-Sol Ea* 113, B08101, doi:10.1029/2007JB005235.

731 Ben-Yosef, E., Tauxe, L., Ron, H., Agnon, A., Avner, U., Najjar, M., Levy, T.E. (2008),  
732 A new approach for geomagnetic archaeointensity research: insights on ancient  
733 metallurgy in the Southern Levant. *J. Archaeol. Sci.* 35, 2863-2879, doi:  
734 10.1016/j.jas.2008.05.016

735 Ben-Yosef, E., Shaar, R., Tauxe, L., Ron, H. (2012), A New Chronological Framework  
736 for Iron Age Copper Production at Timna (Israel). *Bulletin of the American Schools of*  
737 *Oriental Research* 367, 31-71.

738 Ben-Yosef, E., Tauxe, L., Levy, T.E., Shaar, R., Ron, H., Najjar, M. (200), Geomagnetic  
739 intensity spike recorded in high resolution slag deposit in Southern Jordan. *Earth Planet.*  
740 *Sc. Lett.* 287, 529-539, doi: 10.1016/j.epsl.2009.09.001

741 Broadbent, C.P. (1987), Internal structure of solidified iron blast-furnace slag (BFS)  
742 droplets formed by self-impinging jets. *J. Mat. Sci. Lett.* 6, 1264-1266.

743 Cafarella, L., Desantis, A., Meloni, A (1992), Secular Variation in Italy from Historical  
744 Geomagnetic-Field Measurements. *Phys. Earth Planet In.* 73, 206-221, doi:  
745 10.1016/0031-9201(92)90091-9

746 Cartwright, C., Parkington, J. (1997), The wood charcoal assemblages from Elands Bay

747 Cave, Southwestern Cape: Principles, procedures and preliminary interpretation. S. Afr.  
748 Archaeol. Bull. 52, 59-72.

749 Coe, R.S., Gromme, S., Mankinen, E.A. (1978), Geomagnetic Paleointensities from  
750 Radiocarbon-Dated Lava Flows on Hawaii and Question of Pacific Nondipole Low. J.  
751 Geophys. Res. 83, 1740-1756, doi:10.1029/JB083iB04p01740.

752 Day, R., Fuller, M., Schmidt, V.A. (1977), Hysteresis properties of titanomagnetites  
753 grain- size and compositional dependence. Phys. Earth Planet. Inter. 13 (4), 260–267, doi:  
754 10.1016/0031-9201(77)90108-X.

755 Donadini, F., Riisager, P., Korhonen, K., Kahma, K., Pesonen, L., Snowball, I. (2007),  
756 Holocene geomagnetic paleointensities: A blind test of absolute paleointensity techniques  
757 and materials. Phys. Earth Planet In. 161, 19-35, doi: 10.1016/j.pepi.2006.12.002.

758 Dunlop, D.J., Özdemir, Ö. (2001), Rock magnetism: fundamentals and frontiers.  
759 Cambridge University Press.

760 Dunlop, D. J. (2002), Theory and application of the Day plot (Mrs/Ms versus Hcr/Hc), 1.  
761 Theoretical curves and tests using titanomagnetite data, J. Geophys. Res., 107(B3),  
762 doi:10.1029/2001JB000486.

763 Ertepinar, P., Langereis, C.G., Biggin, A.J., Frangipane, M., Matney, T., Okse, T., Engin,  
764 A. (2012), Archaeomagnetic study of five mounds from Upper Mesopotamia between  
765 2500 and 700 BCE: Further evidence for an extremely strong geomagnetic field ca. 3000  
766 years ago. Earth. Planet. Sc. Lett. 357, 84-98, doi: 10.1016/j.epsl.2012.08.039.

767 Fahn, A., Werker, E., Baas, P. (1986), Wood anatomy and identification of trees and  
768 shrubs from Israel and adjacent regions. Israel Academy of Sciences and Humanities.

769 Finlay, C.C., Maus, S., Beggan, C.D., Bondar, T.N., Chambodut, A., Chernova, T.A.,  
770 Chulliat, A., Golovkov, V.P., Hamilton, B., Hamoudi, M., Holme, R., Hulot, G., Kuang,  
771 W., Langlais, B., Lesur, V., Lowes, F.J., Luhr, H., Macmillan, S., Mandea, M., McLean,  
772 S., Manoj, C., Menvielle, M., Michaelis, I., Olsen, N., Rauberg, J., Rother, M., Sabaka,  
773 T.J., Tangborn, A., Toffner-Clausen, L., Thebault, E., Thomson, A.W.P., Wardinski, I.,  
774 Wei, Z., Zvereva, T.I., Wo, I.A.G.A. (2010), International Geomagnetic Reference Field:  
775 the eleventh generation. Geophys. J. Int. 183, 1216-1230, doi: 10.1111/j.1365-

776 246X.2010.04804.x

777 Gallet, Y., Genevey, A., Courtillot, V. (2003), On the possible occurrence of  
778 'archaeomagnetic jerks' in the geomagnetic field over the past three millennia. *Earth*  
779 *Planet. Sc. Lett.* 214, 237-242, doi: 10.1016/S0012-821X(03)00362-5.

780 Gallet, Y., Genevey, A., Le Goff, M., Fluteau, F., Eshraghi, S.A. (2006), Possible impact  
781 of the Earth's magnetic field on the history of ancient civilizations. *Earth Planet Sc. Lett.*  
782 246, 17-26, doi: 10.1016/j.epsl.2006.04.001

783 Genevey, A., Gallet, Y. (2002), Intensity of the geomagnetic field in western Europe over  
784 the past 2000 years: New data from ancient French pottery. *J Geophys. Res.-Sol. Ea.* 107,  
785 doi:10.1029/2001JB000701.

786 Genevey, A., Gallet, Y., Constable, C.G., Korte, M., Hulot, G. (2008), ArcheoInt: An  
787 upgraded compilation of geomagnetic field intensity data for the past ten millennia and  
788 its application to the recovery of the past dipole moment. *Geochem. Geophys. Geosy.* 9,  
789 Q04038, doi:10.1029/2007GC001881.

790 Genevey, A., Gallet, Y., Rosen, J., Le Goff, M. (2009), Evidence for rapid geomagnetic  
791 field intensity variations in Western Europe over the past 800 years from new French  
792 archeointensity data. *Earth Planet Sc. Lett.* 284, 132-143, doi: 10.1016/j.epsl.2009.04.024

793 Genevey, A.S., Gallet, Y., Margueron, J.C. (2003), Eight thousand years of geomagnetic  
794 field intensity variations in the eastern Mediterranean. *J. Geophys. Res.-Sol. Ea.* 108,  
795 2228, doi:10.1029/2001JB001612

796 Gomez-Paccard, M., Chauvin, A., Lanos, P., Dufresne, P., Kovacheva, M., Hill, M.J.,  
797 Beamud, E., Blain, S., Bouvier, A., Guibert, P., Team, A.W. (2012), Improving our  
798 knowledge of rapid geomagnetic field intensity changes observed in Europe between 200  
799 and 1400 AD. *Earth Planet. Sc. Lett.* 355, 131-143, doi: 10.1016/j.epsl.2012.08.037.

800 Ferk, A., Leonhardt, R., Hess, K.-U., Koch, S., Egli, R., Krása, D., Dingwell, D. B.  
801 (2014), Influence of cooling rate on thermoremanence of magnetite grains: Identifying  
802 the role of different magnetic domain states, *J. Geophys. Res., Solid Earth*, 119, 1599–  
803 1606, doi:10.1002/2013JB010845.

804 Gubbins, D. (1987), Mechanism for Geomagnetic Polarity Reversals. *Nature* 326, 167-



805 169, doi:10.1038/326167a0.

806 Gubbins, D., Jones, A.L., Finlay, C.C. (2006), Fall in Earth's magnetic field is erratic.  
807 Science 312, 900-902, doi: 10.1126/science.1124855

808 Halgedahl, S.L., Day, R., Fuller, M. (1980). The effect of cooling rate on the intensity of  
809 weak-field TRM in single-domain magnetite. Journal of Geophysical Research 85. doi:  
810 10.1029/JB085iB07p03690

811 Hext, G.R. (1963), Estimation of Second-Order Tensors, with Related Tests and Designs.  
812 Biometrika 50, 353-373, doi: 10.1093/biomet/50.3-4.353.

813 Hulot, G., Eymin, C., Langlais, B., Manda, M., Olsen, N. (2002), Small-scale structure  
814 of the geodynamo inferred from Oersted and Magsat satellite data. Nature 416, 620-623,  
815 doi:10.1038/416620a.

816 Jelinek, V. (1978), Statistical Processing of Anisotropy of Magnetic-Susceptibility  
817 Measured on Groups of Specimens. Stud Geophys Geod 22, 50-62.

818 Kassianidou, V. (2004), Recording Cyprus's mining history through archaeological  
819 survey. British School at Athens Studies, 95-104.

820 Kirschvink, J.L. (1980), The Least-Squares Line and Plane and the Analysis of  
821 Paleomagnetic Data. Geophys J. Roy. Astr. S. 62, 699-718, doi: 10.1111/j.1365-  
822 246X.1980.tb02601.x.

823 Kovacheva, M., Chauvin, A., Jordanova, N., Lanos, P., Karloukovski, V. (2009),  
824 Remanence anisotropy effect on the palaeointensity results obtained from various  
825 archaeological materials, excluding pottery. Earth Planets Space 61, 711-732.

826 Le Goff, M., Gallet, Y. (2004), A new three-axis vibrating sample magnetometer for  
827 continuous high-temperature magnetization measurements: applications to paleo- and  
828 archeo-intensity determinations. Earth Planet Sc. Lett. 229, 31-43, doi:  
829 10.1016/j.epsl.2004.10.025

830 Levy, T.E., Higham, T., Ramsey, C.B., Smith, N.G., Ben-Yosef, E., Robinson, M.,  
831 Munger, S., Knabb, K., Schulze, J.P., Najjar, M., Tauxe, L. (2008), High-precision

832 radiocarbon dating and historical biblical archaeology in southern Jordan. *P. Natl. Acad.*  
833 *Sci. USA* 105, 16460-16465, doi: 10.1073/pnas.0804950105

834 Malin, S.R.C., Barraclough, D.R. (1982), 150th Anniversary of Gauss 1st Absolute  
835 Magnetic Measurement. *Nature* 297, 285.

836 Manasse, A., and Mellini M. (2002), Chemical and textural characterization of medieval  
837 slags from the Massa Marittima smelting sites (Tuscany, Italy). *J. Cult. Herit.* 3(3), 187-  
838 198, doi: 10.1016/S1296-2074(02)01176-7.

839 Min'ko N.I., Nevedomskii, V.A., Vagin, V.V. (1988), Crystallization in silicomanganese  
840 slag castings. *Glass Ceram.* 45 (3), 114–116.

841 Nagata, T., Momose, K., Arai, Y. (1963), Secular Variation of Geomagnetic Total Force  
842 during Last 5000 Years. *J. Geophys. Res.* 68, 5277-5281.

843 Olson, P. (2002), Geophysics - The disappearing dipole. *Nature* 416

844 Olson, P., Amit, H. (2006), Changes in earth's dipole. *Naturwissenschaften* 93, 519-542.

845 Paterson, G. A., Tauxe, L., Biggin, A. J., Shaar, R., Jonestrask, L. C. (2014), On  
846 improving the selection of Thellier-type paleointensity data. *Geochem. Geophys. Geosy.*  
847 15. doi:10.1002/2013GC005135

848 Paterson, G.A., Heslop, D., Muxworthy, A.R. (2010), Deriving confidence in  
849 paleointensity estimates. *Geochem. Geophys. Geosy.* 11, Q07Z18,  
850 doi:10.1029/2010GC003071.

851 Pike, C. R., A. P. Roberts, and Verosub, K. L. (1999), Characterizing interactions in fine  
852 magnetic particle systems using first order reversal curves, *J. Appl. Phys.*, 85(9), 6660–  
853 6667.

854 Pouchou, J.L., Pichoir, F. (1984), New model for quantitative x-ray microanalysis. Part I:  
855 Application to the analysis of homogeneous samples. *Recherche Aerospatiale (English*  
856 *Edition)*, 3, 13-38.

857 Ramsey, C.B. (2008), Deposition models for chronological records. *Quaternary Sci. Rev.*  
858 27, 42-60, doi: 10.1016/j.quascirev.2007.01.019.

859 Ramsey, C.B. (2009), Bayesian Analysis of Radiocarbon Dates. *Radiocarbon* 51, 337-

860 360.

861 Ramsey, B.C., Lee, S. (2013). Recent and Planned Developments of the Program OxCal.  
862 Radiocarbon, 55(2-3), 720-730.

863 Reimer, P.J., Bard, E., Bayliss, A., Beck, J.W., Blackwell, P.G., Ramsey, C.B., Buck,  
864 C.E., Cheng, H., Edwards, R.L., Friedrich, M., Grootes, P.M., Guilderson, T.P.,  
865 Haflidason, H., Hajdas, I., Hatte, C., Heaton, T.J., Hoffmann, D.L., Hogg, A.G., Hughen,  
866 K.A., Kaiser, K.F., Kromer, B., Manning, S.W., Niu, M., Reimer, R.W., Richards, D.A.,  
867 Scott, E.M., Southon, J.R., Staff, R.A., Turney, C.S.M., van der Plicht, J. (2013), Intcal13  
868 and Marine13 Radiocarbon Age Calibration Curves 0-50,000 Years Cal Bp. Radiocarbon  
869 55, 1869-1887, doi: 10.2458/azu\_js\_rc.55.16947

870 Rogers, J., Fox, J.M.W., Aitken, M.J. (1979), Magnetic-Anisotropy in Ancient-Pottery.  
871 Nature 277, 644-646.

872 Schweingruber, F.H. (1990), Anatomy of European woods. Paul Haupt, Bern and  
873 Stuttgart, Stuttgart.

874 Selkin, P.A., Gee, J.S., Tauxe, L. (2007), Nonlinear thermoremanence acquisition and  
875 implications for paleointensity data. Earth Planet. Sc. Lett. 256, 81-89, doi:  
876 10.1016/j.epsl.2007.01.017

877 Selkin, P.A., Gee, J.S., Tauxe, L., Meurer, W.P., Newell, A.J. (2000), The effect of  
878 remanence anisotropy on paleointensity estimates: a case study from the Archean  
879 Stillwater Complex. Earth Planet. Sc. Lett. 183, 403-416, doi: 10.1016/S0012-  
880 821X(00)00292-2

881 Selkin, P.A., Tauxe, L. (2000), Long-term variations in palaeointensity. Philos. T. Roy.  
882 Soc. A. 358, 1065-1088, doi: 10.1098/rsta.2000.0574.

883 Shaar, R., Ben-Yosef, E., Ron, H., Tauxe, L., Agnon, A., Kessel, R. (2011), Geomagnetic  
884 field intensity: How high can it get? How fast can it change? Constraints from Iron Age  
885 copper slag. Earth Planet. Sc. Lett. 301, 297-306, doi: 10.1016/j.epsl.2010.11.013.

886 Shaar, R., Feinberg, J.M. (2013), Rock magnetic properties of dendrites: insights from  
887 MFM imaging and implications for paleomagnetic studies. Geochem. Geophys. Geosy.  
888 14, 407-421, doi:10.1002/ggge.20053.

889 Shaar, R., Ron, H., Tauxe, L., Kessel, R., Agnon, A., Ben-Yosef, E., Feinberg, J.M.  
890 (2010), Testing the accuracy of absolute intensity estimates of the ancient geomagnetic  
891 field using copper slag material. *Earth Planet. Sc. Lett.* 290, 201-213, doi:  
892 10.1016/j.epsl.2009.12.022

893 Shaar, R., Tauxe, L. (2013), Thellier GUI: An integrated tool for analyzing paleointensity  
894 data from Thellier-type experiments. *Geochem. Geophys. Geosy.* 14, 677-692, doi:  
895 10.1002/ggge.20062

896 Tauxe, L. (2010), *Essentials of Paleomagnetism*. University of California Press,  
897 Berkeley.

898 Tauxe, L., Staudigel, H. (2004), Strength of the geomagnetic field in the Cretaceous  
899 Normal Superchron: New data from submarine basaltic glass of the Troodos Ophiolite.  
900 *Geochem. Geophys. Geosy.* Q02H06, doi:10.1029/2003GC000635.

901 Tauxe, L., Bertram, H. N., Seberino, C. (2002), Physical interpretation of hysteresis loops:  
902 Micromagnetic modeling of fine particle magnetite, *Geochem. Geophys. Geosyst.*, 3(10),  
903 1055, doi:10.1029/2001GC000241.

904 Tauxe, L., T., Y. (2007). *Paleointensities, geomagnetism*.

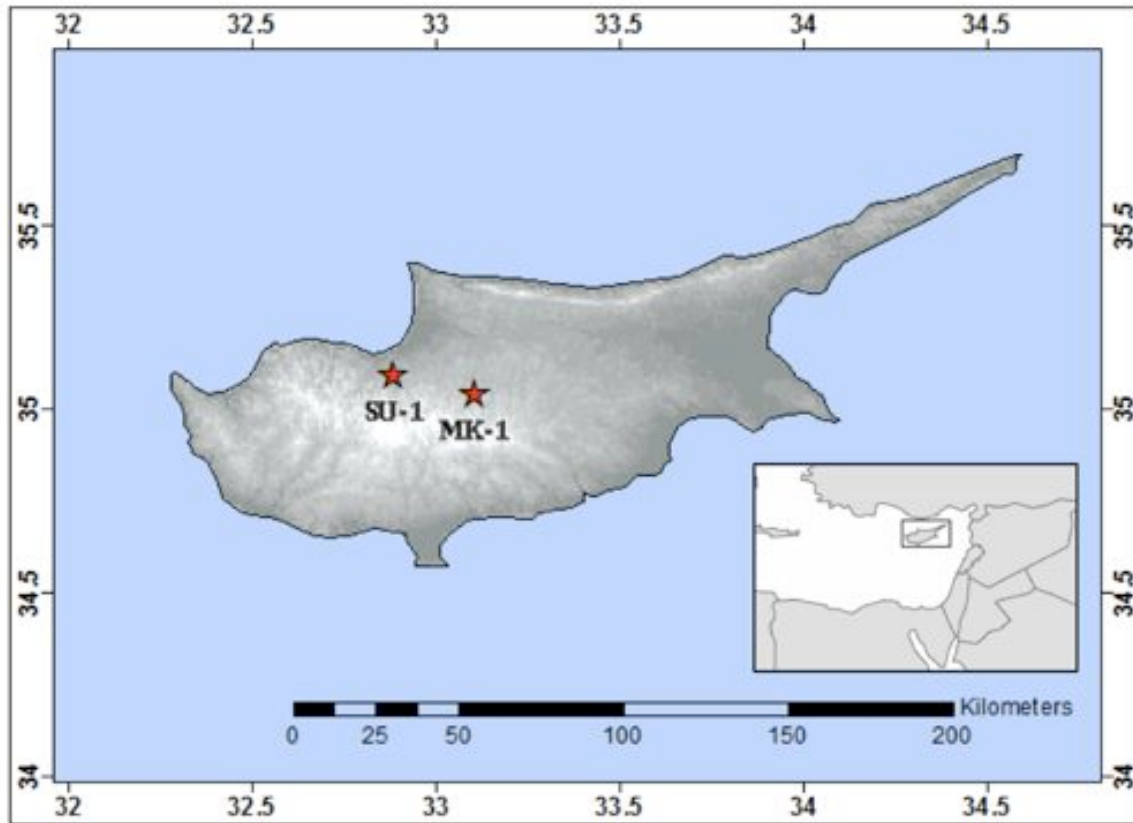
905 Touchan, R., Xoplaki, E., Funkhouser, G., Luterbacher, J., Hughes, M.K., Erkan, N.,  
906 Akkemik, U., Stephan, J. (2005), Reconstructions of spring/summer precipitation for the  
907 Eastern Mediterranean from tree-ring widths and its connection to large-scale  
908 atmospheric circulation. *Clim Dynam* 25, 75-98.

909 Valet, J.P. (2003), Time variations in geomagnetic intensity. *Rev. Geophys.* 41, 1004,  
910 doi:10.1029/2001RG000104.

911 Whitney, D.L., and Evans, B.W. (2010), Abbreviations for names of rock-forming  
912 minerals. *Am. Mineral.* 95, 185-187.

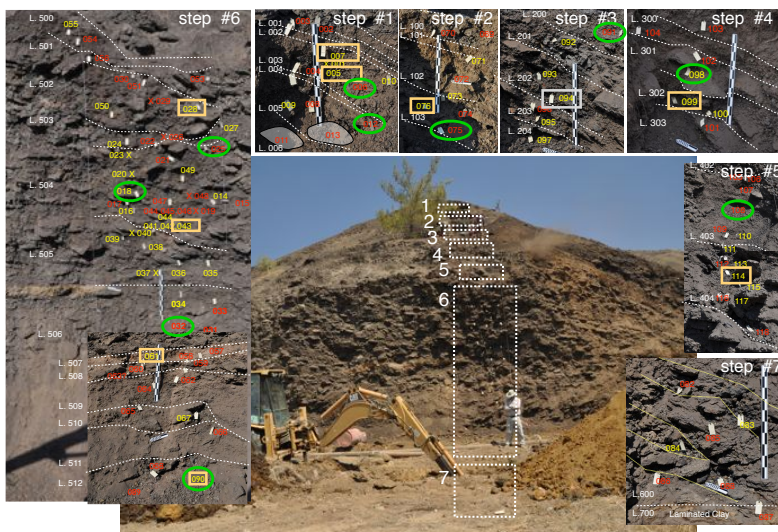
913 Wyderko, M., and Mazanek, E. (1968), The mineralogical characteristics of calcium-iron  
914 olivines. *Mineral. Mag.* 36, 955-961.

915 Zijdeveld, J.D. (1967), A.C. demagnetization of rocks, analysis of results, in: Collinson,  
916 D.W., Creer, K.M., Runcorn, S.K. (Eds.), *Methods in paleomagnetism*. Elsevier, pp. 254–



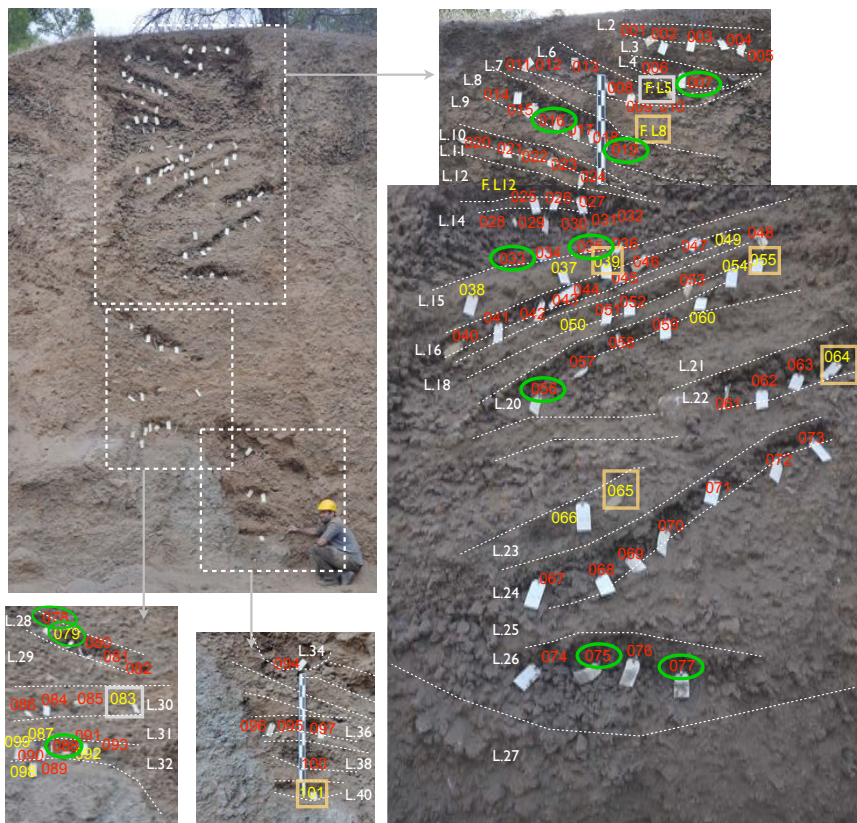
918

919 **Fig. 1.** Location map. SU - Skouriotissa Vouppes, 35.093018°N, 32.885336°E. MK1 -  
920 Mitsero Kokkinoyia, 35.042130°N, 33.106650°E.



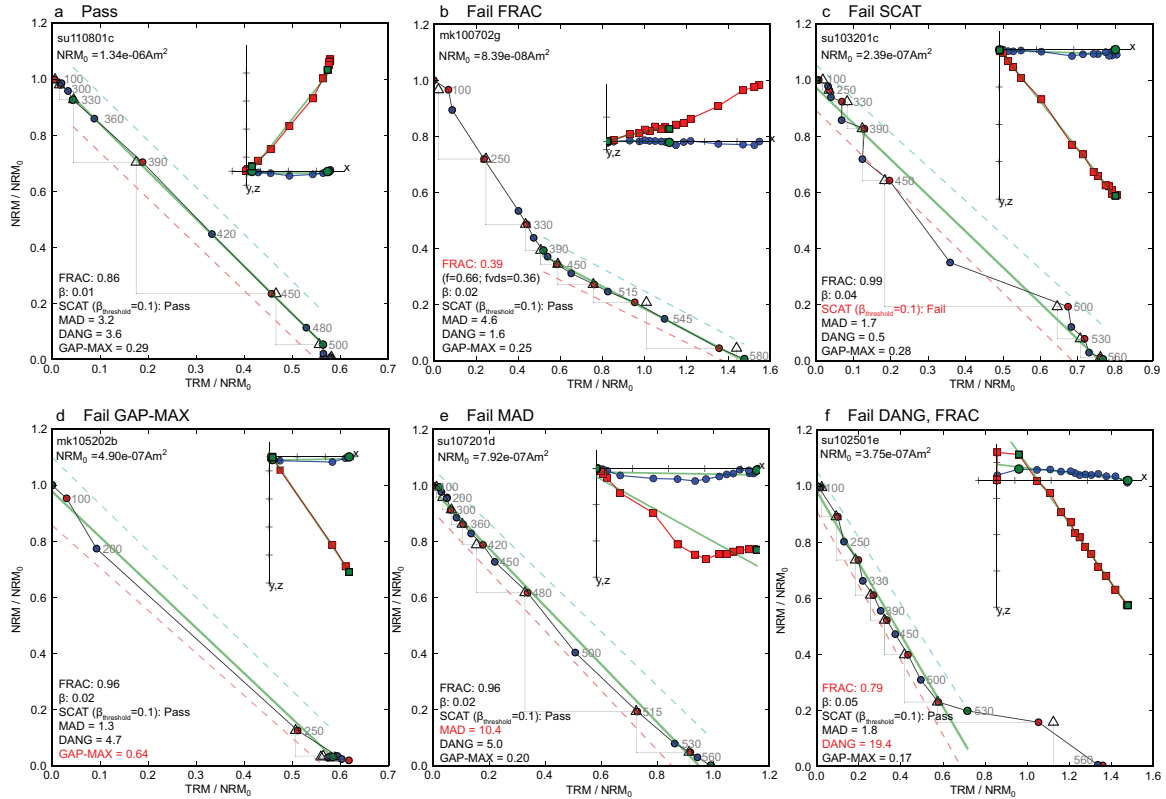
921

922 **Fig. 2.** Slag mound SU1 (Skouriotissa Vouppes). The section is divided into seven  
 923 vertically aligned “steps” and thirty-seven loci (layers). Boundaries between loci are  
 924 marked in dashed white lines and labeled with white numbers. Yellow/red numbers show  
 925 the location of each sampling point in the mound. Locations with charcoal fragments are  
 926 shown in yellow. Dated charcoals are marked with a frame, where gray frame marks the  
 927 charcoal that was not used in the preferred age model. Slag samples that passed the  
 928 selection criteria are marked in green circle.



929  
 930 **Fig. 3.** Slag mound MK1 (Mitsero Kokkinoyia ). Color scheme and numbering is as in  
 931 Fig. 2.





932

933

**Fig. 4:** Examples for different behaviors in the IZZI Thellier type experiments

934

demonstrating our choice for the selection MAD criteria. Red circles, blue circles and triangles

935

in the Arai plots are ZI steps, IZ steps, and pTRM checks, respectively. Blue (red)

936

squares in the Zijderveld plots (insets) are x-y (x-z) projections of the NRMs in specimen

937

coordinate system, where x-axis is rotated to the direction of the NRM. Best-fit lines and

938

temperature bounds are marked in green. Specimen paleointensity statistics are listed in

939

the bottom left corner of the subplots and marked with red if failing our acceptance

940

criteria (Section 2.4). a) Ideal behavior passing all criteria. b) Bi-linear Arai plot resulting

941

with low fraction statistic (*FRAC*) for each linear segment. c) Scattered and zigzaggy plot

942

resulting in high scatter statistic (*SCAT*). Note the misleading low value of  $\beta$ . d) Large

943

gap between points in the Arai plot resulting in high *GAP-MAX* statistic. e) High *MAD*

944

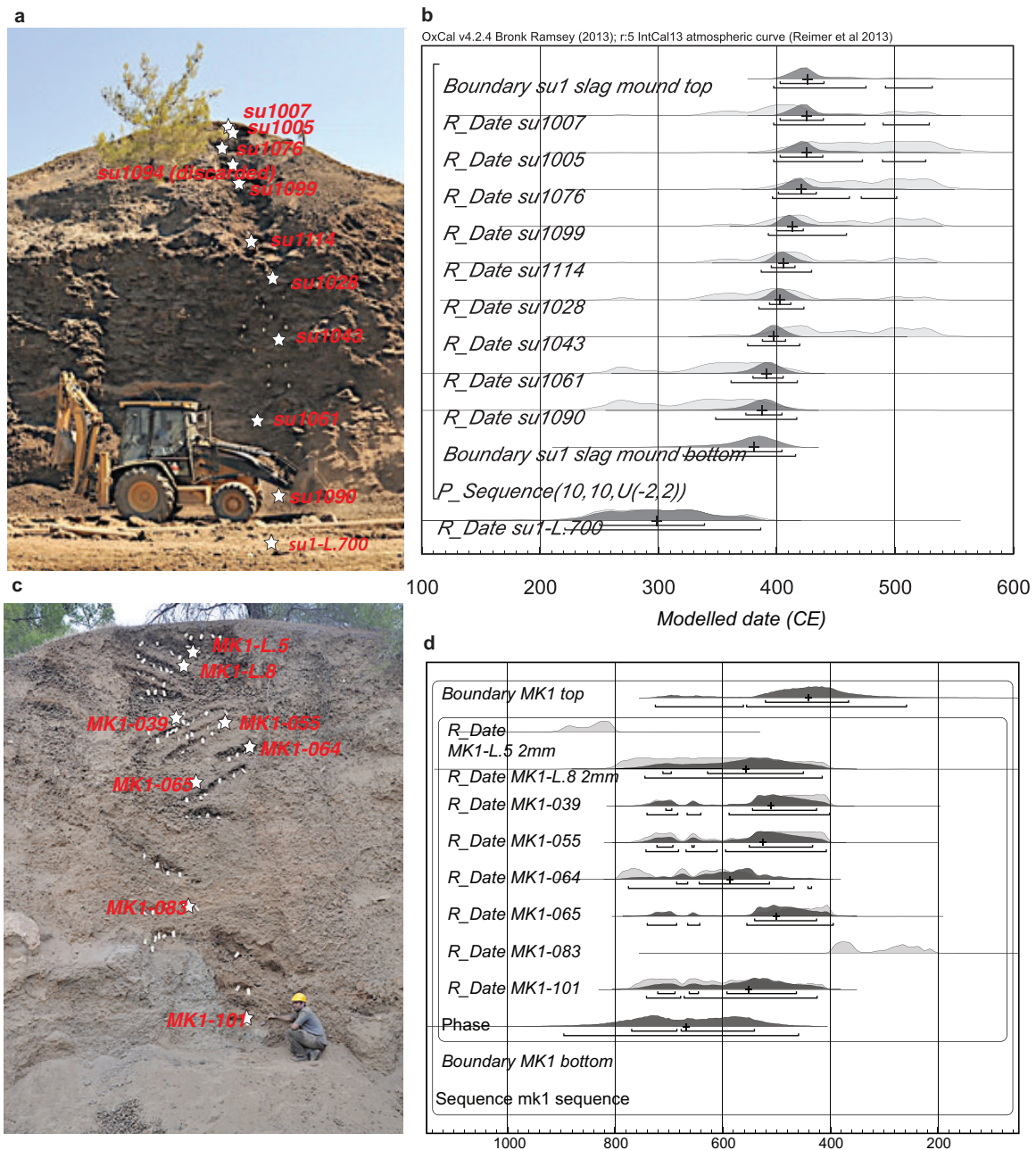
due to non-linear Zijderveld plot, perhaps due to displacement while cooling. f) High

945

*DANG* due to Ziderveld plot not-converging to the origin. For more details on the

946

selection criteria see Section 2.4.



947

948

**Fig. 5:** Radiocarbon data. Stars on the cross sections (a,c) show the location of

949

radiocarbon samples. The exact location is also shown in Figs. 2-3, and the measured

950

stratigraphic height is given in the Supplementary excel file. b,d) Radiocarbon likelihood

951

distributions of the calibrated ages are shown in pale gray. Likelihood distributions of the

952

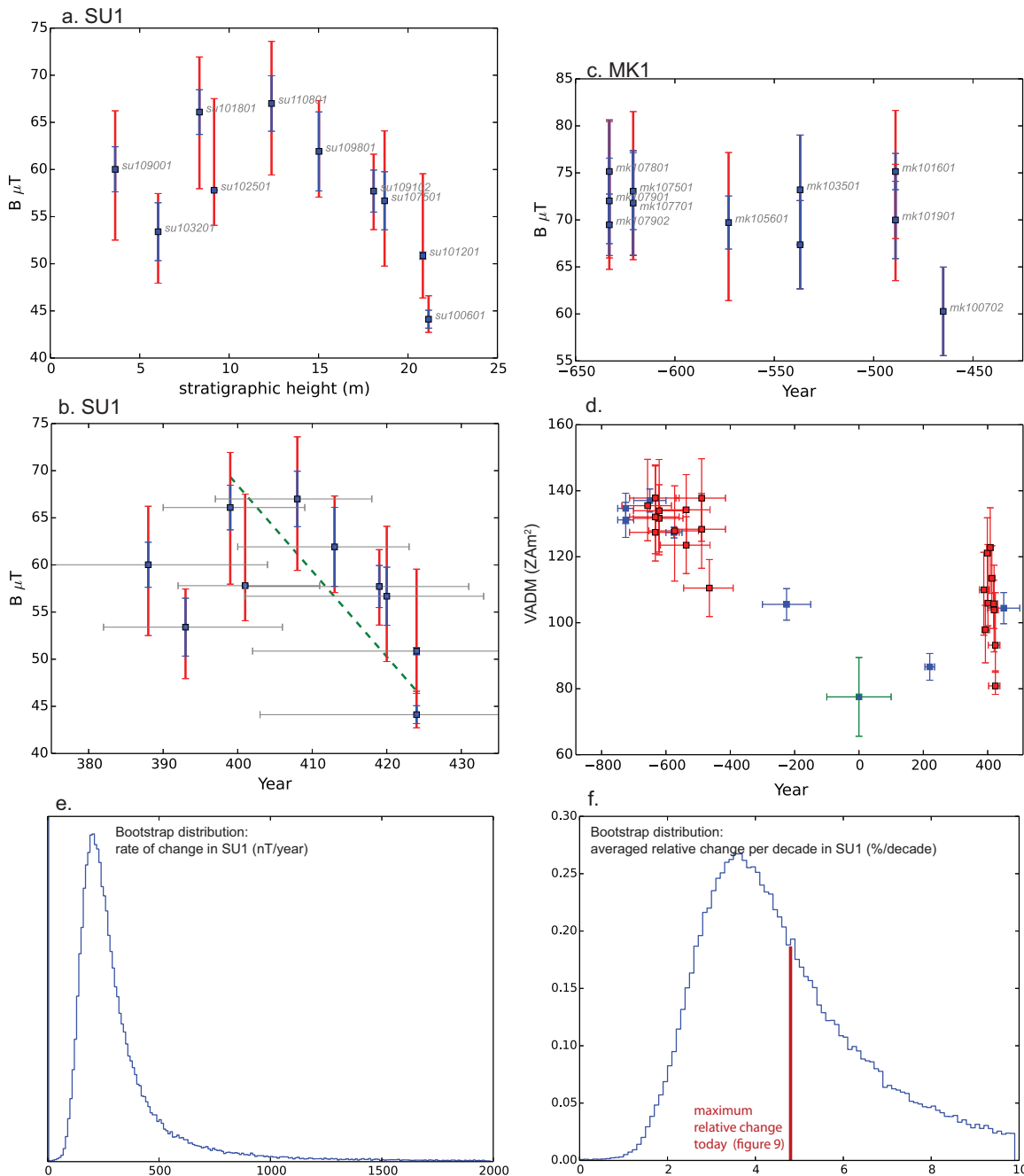
Bayesian modeled ages (Section 3.1) are shown in dark gray. Brackets and crosses

953

represent the 68.2% and the 95.4% probability ranges and the medians. Figure was

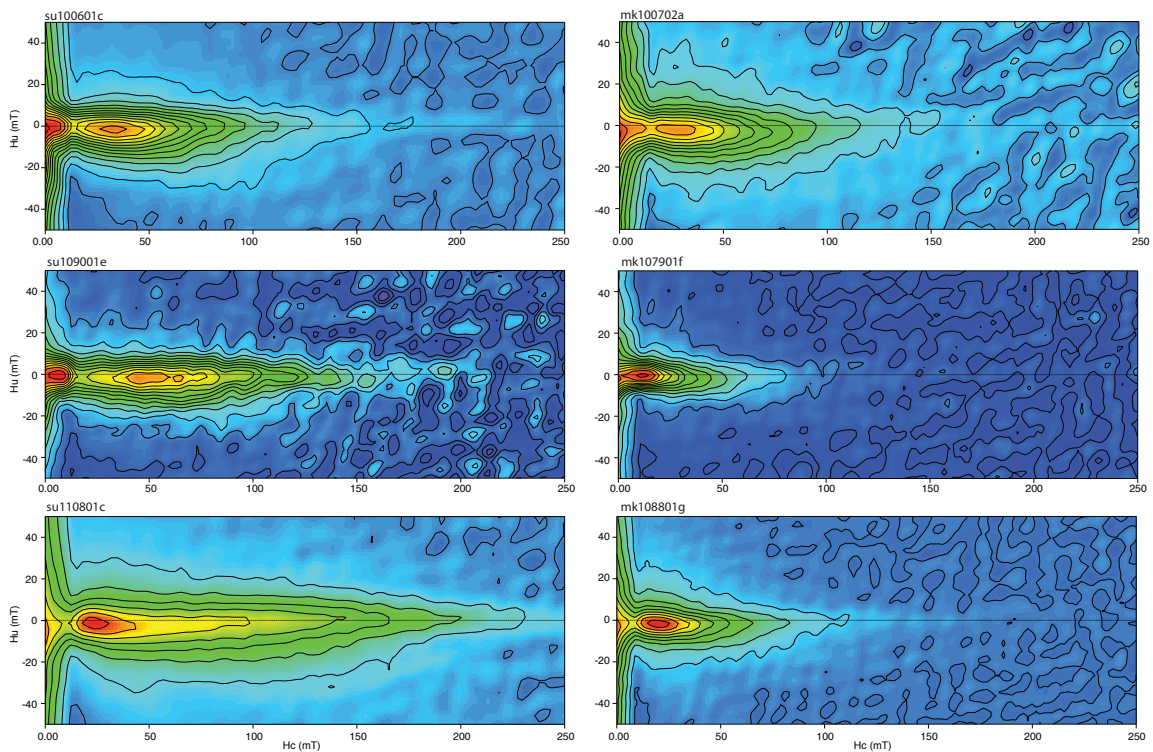


954 produced using OxCal v4.2 program (Ramsey, 2009). For more information see  
 955 Supplementary Material.

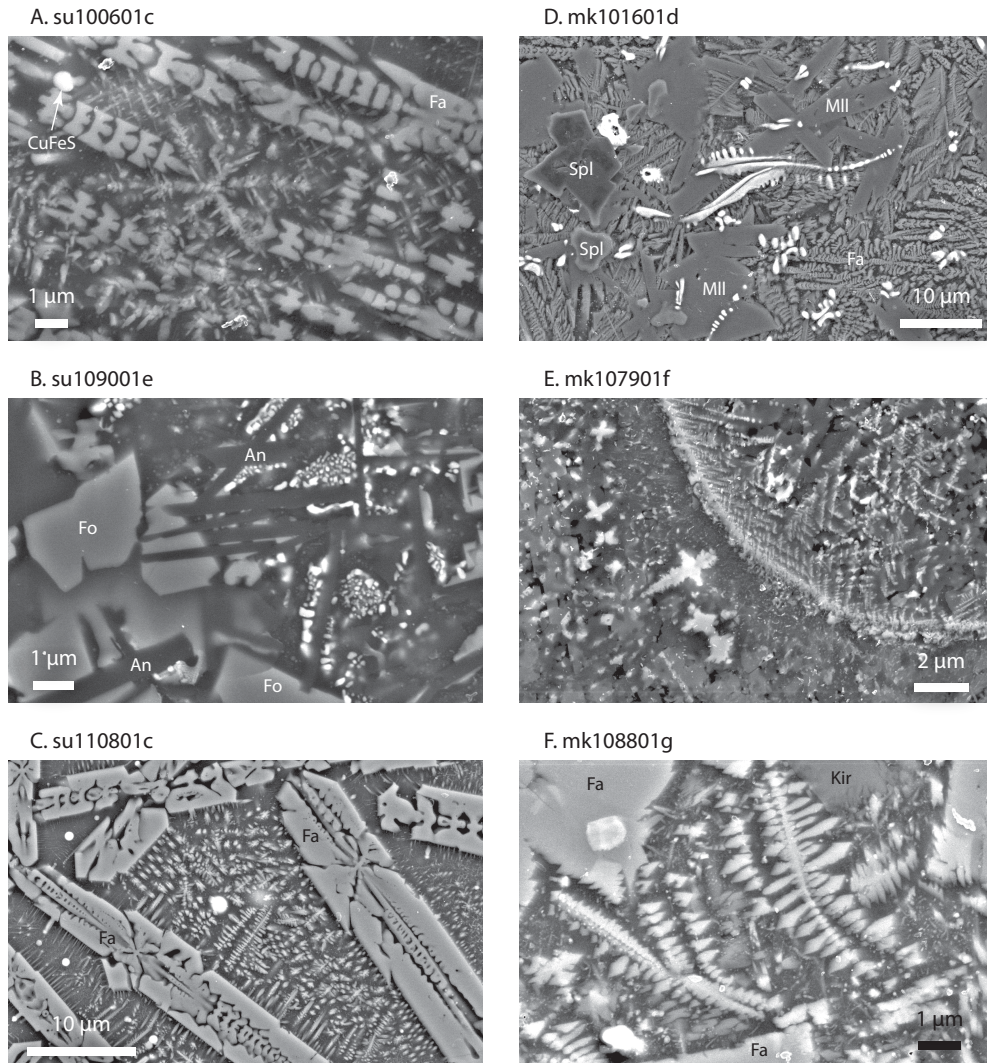


956 **Fig. 6:** Paleointensity plots. a) SU1 paleointensity displayed versus height. b) SU1  
 957 paleointensity displayed versus modeled age. Horizontal error bars in are the 68.2%  
 958 probability range of the modeled ages. Green dashed lines show the weighted least square  
 959 line of the top 8 samples. c) MK1 paleointensity displayed versus modeled age. In a)-c)  
 960

961 the blue vertical error bars are the standard deviations of the STDEV-OPT mean  
962 calculated using the automatic interpretation procedure of the Thellier-GUI (Table 1).  
963 Red error bars show the minimum and the maximum sample means that pass the  
964 acceptance criteria  $\pm$  their standard deviations (See section 3.4 for details). d) VADM  
965 estimates from previous studies: Blue symbols are Genevey et al. (2003) and Gallet et al.  
966 (2006). Green symbol is Ben-Yosef et al. (2008). e,f) bootstrap distributions of the rate  
967 (nT/year) and the relative change (%/decade) calculated using the eight uppermost  
968 samples in SU1.

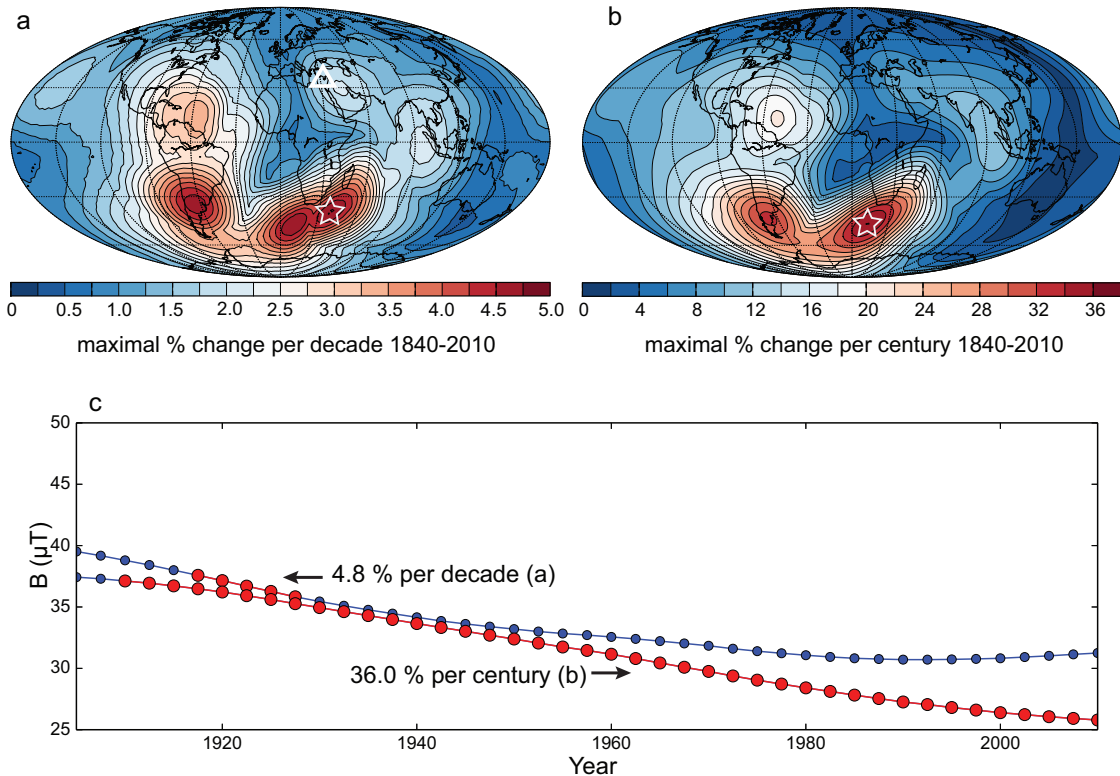


969 **Fig. 7:** FORC distributions produced using FORCinel program (Harrison and Feinberg,  
970 2008). Plots use the same horizontal and vertical scale for comparison.  
971



972  
 973 **Fig. 8.** Representative backscattered electron micrographs of Cypriot slag. (A) Fine  
 974 dendrites of magnetite growing between larger skeletal laths of fayalitic olivine (Fa).  
 975 Light colored grains label (CuFeS) are iron-sulfide minerals. (B) Aggregates of  
 976 submicrometer-sized grains of titanomagnetite occurring between elongated laths of  
 977 anorthitic plagioclase (An). Forsteritic olivine (Fo) and CuFe-sulfide are also present.  
 978 (C) Magnetite dendrites with submicrometer branches nucleating in a crystallographically  
 979 controlled manner from the edges of larger, skeletal fayalitic olivine grains. Bright white  
 980 grains are CuFe-sulfides. Dark grey is glass. (D) Coarse dendrites of magnetite between  
 981 melilite (Mll) and fine fayalite dendrites. Spinel (Spl) grains were common in this

982 sample. (E) Magnetite dendrites nucleating at a quench surface on a fragment of  
 983 preexisting slag. Coarser magnetite dendrites can be seen on the left side of the image  
 984 surrounded by olivine and glass. (F) Magnetite dendrites occurring within the interstitial  
 985 space between fayalite and kirschsteinite (Kir). Mineral abbreviations are from Whitney  
 986 and Evans (2010).



987 **Fig. 9.** Maps of maximal rates of change in the historical field (1840-2010). Relative  
 988 rates ( $100 \cdot \frac{B_{\max} - B_{\min}}{\text{mean}(B_{\max}, B_{\min})}$ ) were calculated using gufm1 model (Jackson et al., 2000)  
 989 from 1840 to 1990 and IGRF models (Finlay et al., 2010) from 1990 to 2010. a)  
 990 Maximum relative rate in a time window of 10 years. b) Maximum relative rate in a time  
 991 window of 100 years. The locations with the highest relative rates are marked with stars.  
 992 Our study area is marked with triangle. The most active areas are confined to narrow  
 993 lobes mostly in the southern hemisphere. Our study area is the same longitudinal band as  
 994 the most active lobe near South Africa. c) Intensity changes in the historical field (1840 –  
 995 2010) plotted at the location marked in stars in (a) and (b).

997

Sample	Mound	Locus or height <sup>a</sup>	Age model <sup>b</sup>			n	Optimal $\sigma$ (STDEV-OPT) <sup>c</sup>		Extended error envelope <sup>d</sup>	
			Median	68.2% low	68.2% high		B $\pm$ $\sigma$	VADM $\pm$ $\sigma$	B( $\mu$ T)	VADM(ZAm <sup>2</sup> )
mk100702		4	-465	-545	-391	8	60.3 $\pm$ 4.7	110.5 $\pm$ 8.6	55.6-65.0	101.9-119.1
mk101601		8	-489	-569	-415	6	75.1 $\pm$ 1.9	137.8 $\pm$ 3.5	68.0-81.6	124.7-149.7
mk101901		8	-489	-569	-415	4	70.0 $\pm$ 4.1	128.3 $\pm$ 7.5	63.5-75.9	116.5-139.2
mk103302		14	-537	-617	-463	4	67.4 $\pm$ 4.7	123.5 $\pm$ 8.6	62.7-72.0	114.9-132.1
mk103501		14	-537	-617	-463	5	73.2 $\pm$ 5.8	134.2 $\pm$ 10.7	67.4-79.0	123.5-144.9
mk105601	mk1	20	-573	-653	-499	4	69.7 $\pm$ 2.8	127.8 $\pm$ 5.2	61.4-77.2	112.6-141.5
mk107501		26	-621	-701	-547	4	73.0 $\pm$ 4.1	133.9 $\pm$ 7.5	65.8-81.5	120.6-149.5
mk107701		26	-621	-701	-547	6	71.8 $\pm$ 5.6	131.6 $\pm$ 10.2	66.2-77.4	121.4-141.8
mk107801		28	-633	-713	-559	6	75.2 $\pm$ 5.5	137.8 $\pm$ 10.0	69.7-80.6	127.7-147.8
mk107901		28	-633	-713	-559	5	72.0 $\pm$ 4.5	132.1 $\pm$ 8.3	66.0-80.5	120.9-147.5
mk107902		28	-633	-713	-559	4	69.5 $\pm$ 3.3	127.4 $\pm$ 6.0	64.7-75.1	118.7-137.7
mk108801		32	-657	-737	-583	8	73.9 $\pm$ 3.2	135.5 $\pm$ 5.9	68.1-81.5	124.8-149.5
su109001		3.63	388	374	404	8	60.0 $\pm$ 2.4	110.0 $\pm$ 4.4	52.5-66.2	96.2-121.4
su103201		6.03	393	382	406	5	53.4 $\pm$ 3.1	97.9 $\pm$ 5.6	47.9-57.4	87.8-105.3
su101801		8.34	399	390	409	8	66.1 $\pm$ 2.4	121.1 $\pm$ 4.3	58.0-71.9	106.2-131.8
su102501 <sup>e</sup>		9.16	401	392	411	4	57.8 $\pm$ 0.1	105.9 $\pm$ 0.1	54.1-67.5	99.1-123.7
su110801	su1	12.37	408	397	418	7	67.0 $\pm$ 2.9	122.8 $\pm$ 5.4	59.4-73.6	108.9-134.8
su109801		15.02	413	400	423	3	61.9 $\pm$ 4.2	113.5 $\pm$ 7.7	57.1-67.3	104.6-123.3
su109102		18.08	419	401	431	5	57.7 $\pm$ 2.2	105.7 $\pm$ 4.1	53.6-61.6	98.3-112.9
su107501		18.69	420	401	433	7	56.7 $\pm$ 3.1	103.9 $\pm$ 5.6	49.8-64.1	91.2-117.5
su101201		20.83	424	402	438	3	50.9 $\pm$ 0.4	93.2 $\pm$ 0.7	46.4-59.6	85.0-109.1
su100601		21.15	424	403	438	4	44.1 $\pm$ 0.9	80.8 $\pm$ 1.7	42.7-46.6	78.3-85.4

<sup>a</sup> Locus number refers to the layer numbering of MK1 in Figure 3. Height is the relative elevation of the samples in SU1 mound.

<sup>b</sup> See section 3.1 and Supplementary Material for age models .

<sup>c</sup> STDEV-OPT is the algorithm in the Thellier GUI program (Shaar and Tauxe, 2013) that choose from all the acceptable means that pass criteria the mean with the minimum  $\sigma$ %. All results are corrected for anisotropy and NLT effects. See section 2.4 for details.

<sup>d</sup> Minimum and maximum means that pass the acceptance criteria  $\pm$  their standard deviation.

<sup>e</sup> Baked clay fragment (tile or furnace wall). Results are corrected for cooling rate effect (see Supplementary Material).

998  
999  
1000  
1001  
1002  
1003  
1004  
1005  
1006  
1007

1008

## 1009 **Supporting Material**

1010 Auxiliary material includes the following:

- 1011 • Excel file with radiocarbon analysis data.
- 1012 • PDF with supplemental figures and tables
- 1013 • TXT file with specimen paleointensity data
- 1014 • MagIC\_README.txt with explanation on how use PmagPy software to view and
- 1015 analyze the MagIC formatted data.

